TU Delft

Delft University of Technology

A Comparative Study of Gas Flooding and Foam-Assisted Chemical Flooding in Bentheimer Sandstones

Janssen, Martijn; Pilus, Rashidah M.; Zitha, Pacelli L.J.

DOI
10.1007/s11242-018-01225-3

Publication date
2019

Document Version
Final published version

Published in
Transport in Porous Media

Citation (APA)
Janssen, M., Pilus, R. M., & Zitha, P. L. J. (2019). A Comparative Study of Gas Flooding and Foam-Assisted Chemical Flooding in Bentheimer Sandstones. *Transport in Porous Media*, *131 (2020)*(1), 101–134. https://doi.org/10.1007/s11242-018-01225-3

Important note
To cite this publication, please use the final published version (if applicable).
Please check the document version above.

Copyright
Other than for strictly personal use, it is not permitted to download, forward or distribute the text or part of it, without the consent of the author(s) and/or copyright holder(s), unless the work is under an open content license such as Creative Commons.

Takedown policy
Please contact us and provide details if you believe this document breaches copyrights.
We will remove access to the work immediately and investigate your claim.

This work is downloaded from Delft University of Technology.
For technical reasons the number of authors shown on this cover page is limited to a maximum of 10.

Transport in Porous Media (2020) 131:101–134
https://doi.org/10.1007/s11242-018-01225-3

A Comparative Study of Gas Flooding and Foam-Assisted Chemical Flooding in Bentheimer Sandstones

Martijn T. G. Janssen[1] · **Rashidah M. Pilus**[2] · **Pacelli L. J. Zitha**[1]

Received: 13 April 2018 / Accepted: 12 December 2018 / Published online: 2 January 2019
© Springer Nature B.V. 2019

Abstract
A laboratory study of principal immiscible gas flooding schemes is reported. Very well-controlled experiments on continuous gas injection, water-alternating-gas (WAG) and alkaline–surfactant–foam (ASF) flooding were conducted. The merits of WAG and ASF compared to continuous gas injection were examined. The impact of ultra-low oil–water (o/w) interfacial tension (IFT), an essential feature of the ASF scheme along with foaming, on oil mobilisation and displacement of residual oil to waterflood was also assessed. Incremental oil recoveries and related displacement mechanisms by ASF and WAG compared to continuous gas injection were investigated by conducting CT-scanned core-flood experiments using n-hexadecane and Bentheimer sandstone cores. Ultimate oil recoveries for WAG and ASF at under-optimum salinity (o/w IFT of 10^{-1} mN/m) were found to be similar [$60 \pm 5\%$ of the oil initially in place (OIIP)]. However, ultimate oil recovery for ASF at (near-)optimum salinity (o/w IFT of 10^{-2} mN/m) reached $74 \pm 8\%$ of the OIIP. Results support the idea that WAG increases oil recovery over continuous gas injection by drastically increasing the trapped gas saturation at the end of the first few WAG cycles. ASF flooding was able to enhance oil recovery over WAG by effectively lowering o/w IFT ($< 10^{-1}$ mN/m) for oil mobilisation. ASF at (near-)optimum salinity increased clean oil fraction in the production stream over under-optimum salinity ASF.

Keywords Alkaline · Surfactant · Foam · Oil · Immiscible gas injection · Water-alternating-gas · Enhanced oil recovery

1 Introduction

Gas injection has been extensively applied over the years for pressure maintenance in pressure-depleted hydrocarbon reservoirs. However, nowadays, gas injection is mainly con-

✉ Martijn T. G. Janssen
M.T.G.Janssen@tudelft.nl

[1] Petroleum Engineering Department, Delft University of Technology, 2628 CN Delft, The Netherlands

[2] Petroleum Engineering Department, University Teknologi Petronas, 32610 Seri Iskander, Perak, Malaysia

sidered a recovery technique, similarly to water flooding, which is applied during secondary or tertiary recovery stages in the development of an oil field. Either natural or non-natural gas may be injected into mature oil fields for improving oil recovery.

Gas injection processes can be either miscible, where injected gas and displaced oil form a single phase, or immiscible, where distinct gas and liquid phases are preserved even though gas may dissolve partly into the oleic phase. Gasses with low minimum miscibility pressures (MMP) [e.g. carbon dioxide (CO_2)], light hydrocarbon-based oils and high reservoir pressures all favour miscibility. Miscibility leads to oil swelling, oil viscosity reduction and/or oil–water (o/w) interfacial tension (IFT) reduction which promote oil displacement (Lake 1989). However, rock–fluid and fluid–fluid interactions control oil displacement in immiscible gas flooding processes. Unstable displacement due to unfavourable mobility ratio between injected gas and displaced fluids is one of the major drawbacks of any continuous gas injection scheme. Early gas breakthrough due to viscous fingering, gravity segregation and channelling through high permeability streaks are common observations in the laboratory and in the field (Zhu et al. 2004; Rossen et al. 2006; Farajzadeh et al. 2009, 2010; Andrianov et al. 2011).

Water-alternating-gas (WAG), i.e. the injection of gas slugs alternated by water slugs, might delay gas breakthrough considerably leading to a substantial improvement in oil recovery. Unfortunately, gravity segregation might also occur during WAG injection (Andrianov et al. 2011; Talebian et al. 2014). Foaming of the gas is another, potentially more effective, way for improving gas sweep efficiency. Foam reduces gas mobility greatly by trapping gas in a discontinuous form within a continuous liquid phase (Kovscek and Radke 1994; Rossen 1996; Zitha et al. 2006; Du et al. 2007; Zitha and Du 2010; Simjoo et al. 2013). Foam stability is primarily a function of the thickness of thin liquid films, i.e. lamellae, that separate the gas bubbles (Lake 1989; Farajzadeh et al. 2010). Lamellae stability depends mainly on the type of gas used and on the chemical formulation of the continuous aqueous phase (Aronson et al. 1994; Shabib-asl et al. 2014). For instance, higher aqueous solubility of CO_2 compared to nitrogen gas (N_2) has a large impact on foam behaviour.

Mobilising oil trapped in porous media by capillary forces after extensive water flooding is an essential requirement for any successful enhanced oil recovery (EOR) process. Achieving this entails effectively altering the physical properties of reservoir fluids. Immiscible gas flooding might change fluid–fluid interactions and subsequently support oil being displaced through film flow (Khorshidan et al. 2016). In chemical EOR processes, specially designed surfactant slugs are able to lower the o/w IFT significantly, thus mobilising residual oil (Kang et al. 2010; Hirasaki et al. 2011; Guo et al. 2012; Jong et al. 2016). For a fixed surfactant concentration, the magnitude of o/w IFT lowering depends on various parameters of which the aqueous phase salinity is likely to be the most important (Winsor 1954). At optimum salinity, a distinct micro-emulsion phase co-exists with excess water and oil. This Type III system is characterised by an ultra-low o/w IFT. At under-optimum salinity, an oil-in-water micro-emulsion co-exists with excess oil (Type II- system). Finally, at over-optimum salinity a water-in-oil micro-emulsion is in equilibrium with excess water (Type II + system).

Recently, we have investigated the alkaline–surfactant–foam (ASF) flooding process based upon the injection of an alkaline–surfactant (AS) slug for oil mobilisation followed by co-injection of gas and AS drive solution for foam generation, i.e. mobility control (Guo et al. 2012; Hosseini-Nasab and Zitha 2015; Janssen et al. 2018). The alkali in ASF converts naphthenic acids, commonly present in crude oils, into soaps through a saponification process (Chatterjee and Wasan 1998). The synergistic action of these natural surfactants in combination with the added surfactant is responsible for the reduction of the o/w IFT (up to four orders of magnitude) to ultra-low values. Alkali also reduces anionic surfactant adsorption on charged clay sites within sandstones (Hirasaki and Zhang 2004). The ASF process is similar

to the more conventional alkaline–surfactant–polymer (ASP) process. However, ASP uses polymers for mobility control instead of foam (Liu et al. 2008). Unlike ASF, ASP suffers from limitations regarding the use of polymers in high-temperature, high-salinity and low-permeability regions (Shupe 1981). Variants of the ASF process were investigated by others in the literature (Srivastava et al. 2009; Szlendak et al. 2013; Tang et al. 2014; Jong et al. 2016), but they did not provide clues about oil mobilisation and displacement mechanisms.

This paper reports on a systematic comparison of immiscible gas, WAG and ASF flooding based on (CT-scanned) core-flood experiments as a detailed extension of the earlier work of Janssen et al. (2018). It focuses on (a) the beneficial effects of ASF over the more conventional non-chemical EOR methods, (b) the impact of AS slug salinity on oil bank formation and (c) the ability of generated foam to displace the mobilised oil bank. This study includes drive foam stability and AS slug phase behaviour tests and a series of CT-scanned immiscible gas/WAG/ASF core-flood experiments performed in Bentheimer sandstones. ASF core-floods were performed both at under-optimum and at (near-)optimum salinity conditions to investigate its effect on oil bank formation and displacement by foam. The paper proceeds with the Experimental methods, Results, Discussion and Conclusions.

2 Experimental Methods

2.1 Chemicals

Table 1 presents the physical properties of the chemicals used in this study. The oil used to conduct the core-floods was n-hexadecane. A fat-soluble dye (Oil Red O) was added to the oleic phase for ease of visual inspection. In four experiments, the oleic phase was doped with 1-iododecane for enhancement of the CT contrast between the oleic and aqueous phases. Brine was prepared by dissolving sodium chloride in demineralised water. Demineralised water was produced by using an ELGA PURELAB Prima120 water treatment device. It purifies water by using several stages of membrane filtration, to remove most of the mineral and salt ions present, until a water conductivity of 1.0 μS/cm or lower is reached. In two experiments, the model brine was doped with potassium iodide (KI) for enhancing CT visualisation. The AS slug solution was prepared by adding the required amounts of an Internal Olefin Sulfonate (IOS2024) surfactant, a co-solvent (sec-butanol) and an alkaline (sodium carbonate) to brine. The critical micelle concentration (*c.m.c.*) of IOS2024, in the presence of the designed AS slug formulation, equalled approximately 3.0×10^{-3} weight percent (wt%) active matter (AM) IOS2024. The alkali was added to the AS slug solely for minimising surfactant adsorption. The co-solvent was used as a precautionary measure to guarantee stable AS slug solution, even though it is not strictly required when working with IOS2024 below 60 °C (Hirasaki et al. 2011). The defined AS drive formulation is similar to the AS slug composition without the addition of the co-solvent. Nitrogen gas (N_2) was used for continuous gas injection, WAG and for co-injection with AS drive solution for foam generation. All liquid solutions were degassed under vacuum prior to injection.

2.2 Core Samples

Bentheimer sandstones were used in this study as a model reservoir owing to its high permeabilities (2.6 ± 1.2 Darcy) and fairly homogeneous mineralogy (>91 wt% quartz) (Peksa

Table 1 Physical properties of the chemicals used

Chemical	Formula	Molecular weight (g/mol)	Density (g/cm^3)[a]	Viscosity (mPa s)[a]	Supplier	Purity (%)
n-hexadecane	$CH_3(CH_2)_{14}CH_3$	226.45	0.775 ± 0.001	3.365 ± 0.055	Merck	≥ 99
Oil Red O	$C_{26}H_{24}N_4O$	408.49	–	–	Sigma-Aldrich	≥ 75
Sodium chloride[b]	NaCl	58.44	2.160 ± 0.001	–	Merck	≥ 99
Sodium carbonate[b]	Na_2CO_3	105.99	2.540 ± 0.001	–	Sigma-Aldrich	≥ 99
Sec-butanol	$C_4H_{10}O$	74.12	0.806 ± 0.001	–	Merck	≥ 99
1-Iododecane	$CH_3(CH_2)_9I$	268.18	1.257 ± 0.001	–	Sigma-Aldrich	≥ 98
Potassium iodide[b]	KI	166.00	3.120 ± 0.001	–	Sigma-Aldrich	≥ 99
IOS2024	–	–	0.996 ± 0.001	–	Shell Global	19
Nitrogen[b]	N_2	28.01	$1.165 \pm 0.001 \times 10^{-3}$	$1.760 \pm 0.500 \times 10^{-2}$	–	100

[a]All densities and viscosities mentioned are at 20 °C and 1 atmosphere
[b]Lide (2012)

Table 2 Properties of Bentheimer sandstone cores used in this study

	Experiment				
	1	2	3	4	5
Porosity (%)	22.70 ± 0.10	23.10 ± 0.10	23.60 ± 0.10	24.00 ± 0.40	24.00 ± 0.40
Permeability (Darcy)	2.68 ± 0.08	1.94 ± 0.14	2.30 ± 0.18	3.20 ± 0.11	3.45 ± 0.15
Length (cm)	17.00 ± 0.10	17.00 ± 0.10	17.00 ± 0.10	96.20 ± 0.10	97.10 ± 0.10
Diameter (cm)	3.90 ± 0.10	3.90 ± 0.10	3.90 ± 0.10	3.80 ± 0.10	3.80 ± 0.10
Pore volume (cm^3)	46.10 ± 2.89	46.91 ± 2.94	47.93 ± 3.00	261.84 ± 18.85	264.29 ± 18.16

et al. 2015). Newly cored sandstone samples were dried in an oven at 60 °C for 48 h before they were casted into an epoxy resin, to avoid any bypassing flow alongside the core. The resin penetrated approximately 1.00 mm radially into the sandstone, reducing its effective diameter to 3.80 ± 0.10 cm. Multiple equidistant holes were drilled in the glued cores for pressure(drop) measurements. Table 2 gives an overview of the physical properties of the Bentheimer sandstone cores used in this study. Porosities were determined from CT scan data and by using an Ultra Pycnometer 1000 (Quantachrome Corporation).

Short cores with a length of 17.00 ± 0.10 cm were used to perform continuous gas injection and WAG core-flood experiments. These short-core experiments were conducted under stable gravity conditions by placing the core-holder vertically. Longer cores, having a length of 96.65 ± 0.45 cm, were used to conduct the ASF experiments. They were placed horizontally on the couch of the CT scanner. This core length proved to be sufficient for reducing the capillary entry/end effects and, more significantly, for accurate assessment of the oil bank formation and its displacement by foam.

2.3 Experimental Set-up

Figure 1 presents the schematics of the two experimental set-ups that were designed to conduct the core-floods experiments. Set-up A was used to perform the core-flood experiments with the short cores (Exp. 1, 2 and 3), whereas set-up B was used to conduct the experiments with the long cores (Exp. 4 and 5). For both set-ups, the sandstone cores were placed in a specially designed core-holder made of polyether ether ketone (PEEK) characterised by low X-ray attenuation and high mechanical strength. During the experiment, the cores were continuously exposed to a confining pressure equal to the inlet pressure. A dual-cylinder liquid pump (Quizix QX-6000 or QX-1500 HC), mounted in line with the core-holder, was used for injecting aqueous solutions. Either an ISCO pump or a transfer vessel was used for oil injection. A backpressure regulator (DEMO-TU Delft) was installed to control the outlet pressure. A mass flow controller (Bronkhorst, EL-FLOW) was used to set the flowrate of N_2, supplied from a 200-bar cylinder. Multiple absolute and differential pressure transducers were used to record the pressure(drop) along the core. Thermocouples were used for temperature monitoring. The thermocouples and pressure transducers were connected to a data acquisition system (National Instruments, USB-6211) which recorded both parameters using a 10-s time interval. Fluids were either collected in a measuring cup that was placed on a digital balance (Exp. 4 and 5) or by using a fraction collector (GE Akta Frac-920) (Exp. 1, 2 and 3). CO_2, supplied in a 200-bar

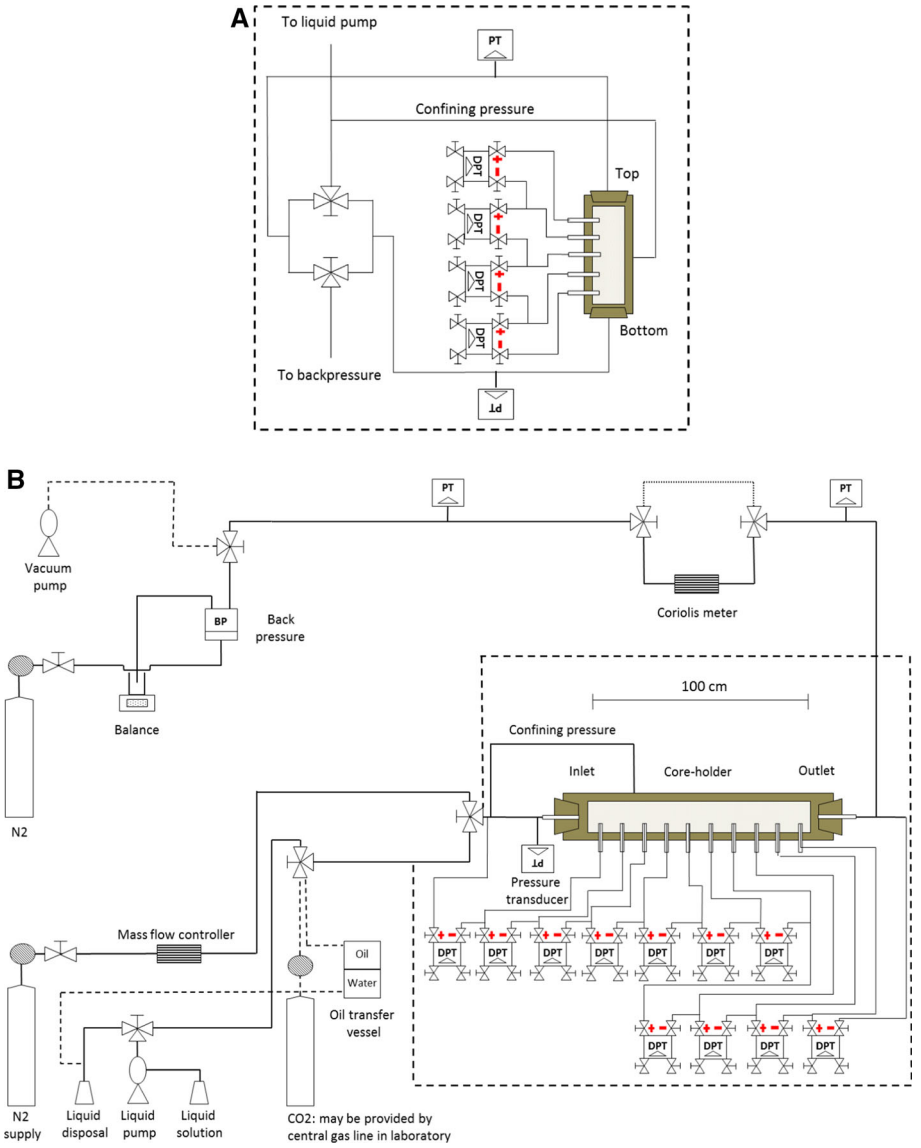

Fig. 1 Schematics of the experimental set-ups. Set-up **a** was used to conduct the baseline experiments (Exp. 1, 2 and 3) with the short cores while set-up **b** was used for performing the ASF experiments (Exp. 4 and 5) using the long cores. In order to switch from set-up **b** to **a** the parts surrounded by dashed lines were substituted. Note that the valves shown in schematic **a** were used for changing the flow direction (either from top-down or from bottom-up)

cylinder, was used for initial flushing of the core (see Sect. 2.5.3). In the ASF core-floods (Exp. 4 and 5), a Coriolis flowmeter (Bronkhorst, CORI-FLOW) was installed at the outlet for measuring effluent densities and mass flow rates. It was used for precisely establishing breakthrough times. All experiments were conducted at ambient temperature (22 ± 2 °C).

Table 3 CT scan settings

Specification		
Tube voltage (kV)	80	140
Tube current (mA)	550	250
Slice thickness (mm)	2.0	2.0
Pixel size (mm × mm)	0.2 × 0.2	0.2 × 0.2
Scan mode	Spiral	Spiral

2.4 CT Scan

During Exp. 2, 3, 4 and 5, the sandstone cores were CT-scanned using a Siemens SOMATOM Definition CT scanner with true dual-energy scanning capabilities. Unfortunately, CT scans acquired during Exp. 2 and 3 suffered from too much artefacts and provide no meaningful insights. Hence, we will only present the CT scans for Exp. 4 and 5. CT scans were taken using simultaneously two X-ray tubes with 80 kV and 140 kV voltage, respectively. True dual-energy scanning is required for quantifying three-phase saturations (Table 7). Table 3 presents the CT scan settings applied.

A single CT scan taken consisted of 490 slices, containing 512 × 512 pixels each. However, the core only occupied part of the slice surface (11 ± 1%). The maximum percentage errors in obtained oil saturations $\left(\frac{\delta S_o \times 100}{S_o}\right)$ and porosities $\left(\frac{\delta \phi \times 100}{\phi}\right)$ using 140 kV data equalled approximately 3.6% and 1.2%, respectively, assuming absolute errors in Hounsfield units (HU) measurements of ± 2 HU at all times (Castanier 1988). The maximum percentage error in derived oil saturations for three-phase conditions equalled roughly 6.9%. Note that in following parts of this paper the errors shown corresponding to parameters obtained by CT data processing are related to standard deviations of the respective dataset and not to the error in CT measurements itself. The data were analysed and visualised using ImageJ software.

2.5 Experimental Procedure

2.5.1 Phase Behaviour and IFT Measurements

Nine combinations of n-hexadecane–AS slug formulations were prepared to assess the systems phase behaviour. The aqueous phase contained 0.3 wt% AM IOS2024, 1.0 wt% Na_2CO_3, 0.5 wt% sec-butanol and NaCl concentrations varying from 0.0 to 2.5 wt%. After their preparation, the n-hexadecane–AS slug mixtures were extensively mixed and placed on a shaking roller for 10 h. Then they were stored in an oven at 90 °C for 4 weeks. The elevated temperature helped accelerate the equilibration process. Once equilibrium was reached, a spinning-drop tensiometer (SVT20N, Dataphysics) was used for measuring o/w IFTs also at 90 °C. For each n-hexadecane–AS slug system, excess brine was extracted and used as a continuous phase and subsequently one single droplet of excess oil was added to the test tube. The shape of the oil droplet as function of revolutions per minute (rpm) was analysed and fitted by the software using the Young–Laplace equation (Young 1805; Laplace 1806). Once the applied centrifugal forces reach equilibrium with the interfacial forces, the droplet's shape will be fixed and unique for a specific o/w IFT. The spinning-drop tensiometer requires oil and water phase densities and the refractive index (RI) of the aqueous phases as input. Note that the

RI for the aqueous phases was assumed to be constant and equalled 1.33 (Hecht 2001). IFTs were measured using a range of rotational speeds of 1000–5000 rpm.

2.5.2 Bulk Foam Stability

Bulk foam experiments were conducted using the Foam Scan apparatus (I.T. Concept-TECLIS) to investigate foam stability of various AS drive formulations. The effect of surfactant concentration and salinity on foam stability in bulk was examined. Fixed volumes of surfactant solution (33.5 ± 0.5 cm^3) were placed in the sample holder after which N_2 was injected through the solution (at 20 cm^3/min) until the foam column reached a volume of 110 ± 1 cm^3. Subsequently, N_2 injection was shut off, and the foam volume was monitored as function of time. The experiments were done at room temperature (21 ± 1 °C), atmospheric pressure and in the absence of oil.

2.5.3 Core-Flood Experiments

An overview of the core-flood experiments conducted in this study is presented in Table 4. The first three experiments, continuous immiscible gas flooding (GF), water flooding followed by immiscible gas flooding (WF + GF) and WAG, serve as baseline core-floods in order to study the incremental efficiency of ASF over immiscible gas flooding and WAG. In the two ASF core-floods, first approximately 0.46 pore volume to liquid (PV) AS slug was injected prior to co-injection of AS drive with N_2 for drive mobility control. The drive foam quality (i.e. gas fractional flow) was kept constant at 57% as this quality proved to be able to generate stable drive foam in the presence of residual oil (Janssen et al. 2018). AS slug injection in Exp. 4 and 5 was done at under-optimum and (near-)optimum salinity conditions, respectively.

The sequence used for conducting the core-flood experiments is presented in Table 5. First air was removed from the core by flushing it with CO_2 for over 2 h. Next, the system was evacuated to roughly − 1 bar before approximately 10 PV of NaCl based brine were injected. The first PV of brine was injected at atmospheric pressure. Afterwards, the backpressure was increased to 25 bar to ensure complete dissolution of CO_2 in brine and full core saturation with brine. At the end of brine injection, flowrates were varied in order to determine the absolute permeability to brine using Darcy's law (Darcy 1856). Following brine injection, circa 3 PV of n-hexadecane were injected (primary drainage) until no more water was produced from the core. This established the connate water saturation (S_{wc}) and, correspondingly, the initial oil saturation (S_{oi}). Thereafter either continuous gas (Exp. 1) or WAG (Exp. 3) injection was done. In the latter, a total of 12 WAG cycles were injected, each cycle started with injecting 1.30 ± 0.02 PV of N_2 followed by 0.22 ± 0.02 PV of water. In the other core-floods, nearly 7 PV of NaCl brine were injected (water flooding) subsequent to primary drainage. During the last PV of injection, the water injection rate was raised by a factor 16 (bump flood) to minimise the capillary end effect (Huang and Honarpour 1998) and thus ensuring that residual oil to waterflood (S_{or_WF}) was actually reached in Exp. 4 and 5. In order to obtain the oil and water end-point relative permeabilities (k^*_{ro} and k^*_{rw}) by using Darcy's law, oil and water injection rates were varied at the end of primary drainage and water flooding, respectively. After water flooding, either gas flooding (Exp. 2) or ASF flooding (Exp. 4 and 5) was done.

The continuous gas injection (Exp. 1 and 2) and WAG flooding (Exp. 3) core-floods were performed under gravity stable conditions by positioning the core vertically and injecting water bottom-up and oil/gas top-down. In the WAG experiment, all phases were injected top-down. For the ASF experiments (Exp. 4 and 5), first an AS slug (0.46 PV) was injected

Table 4 Overview of core-flood experiments conducted

Exp.	EOR method	Gas flow rate (cm^3/min)	Liquid flow rate (cm^3/min)	WAG ratio (water–gas ratio)	AS slug formulation (wt%)	AS drive formulation (wt%)	Drive foam quality (%)	Backpressure (bar)	CT
1	GF	0.500	–	–	–	–	–	10	No
2	WF + GF	0.500	2.000	–	–	–	–	5	No
3	WAG	0.500	2.000	1:6	–	–	–	5	No
4	ASF	0.627	0.473	–	NaCl (0.4) Na_2CO_3 (1.0) Sec-butanol (0.5) IOS2024 (0.3)	NaCl (0.4) Na_2CO_3 (1.0) IOS2024 (0.3)	57	20	Yes[a]
5	ASF	0.627	0.473	–	NaCl (2.0) Na_2CO_3 (1.0) Sec-butanol (0.5) IOS2024 (0.3)	NaCl (2.0) Na_2CO_3 (1.0) IOS2024 (0.3)	57	20	Yes[a]

In experiments 1 and 3, the EOR process was initiated at connate water saturation (i.e. initial oil saturation), whereas in the other core-floods, either gas flooding or ASF was applied at residual oil saturation to waterflood

[a]In experiment 4 and 5, the oleic phase was doped with 25 wt% and 20 wt% 1-iododecane, respectively

Table 5 Sequence of experimental procedure

Step	Experiment	Description	Backpressure (bar)	Flow rate (cm^3/min)	Injection pressure (bar)	Flow direction (Exp. 1, 2 and 3)
1	All	CO_2 flush	0	–	5	Down
2	All	Vacuuming	0	–	–	–
3	All	Brine saturation	0, 25	Exp. 1, 2, 3 = 2.000 Exp. 4, 5 = 0.500	–	Up
4	All	Oil injection	Exp. 1, 2, 3 = 0 Exp. 4, 5 = 20	Exp. 1, 3 = 2.000 Exp. 2 = 5.000 Exp. 4 = 0.500 Exp. 5 = 0.200	–	Down
5	Exp. 2, 4, 5	Water flooding[a]	Exp. 2 = 0 Exp. 4, 5 = 20	Exp. 2 = 2.000 Exp. 4, 5 = 0.250	–	Up
6	Exp. 1, 2	Gas flooding	Exp. 1 = 10 Exp. 2 = 5	0.500	–	Down
7	Exp. 3	WAG injection[a]	5	Gas: 0.500 Water: 2.000	–	Down
8	Exp. 4, 5	AS slug injection	20	0.150	–	–
9	Exp. 4, 5	AS drive co-injection	20	Gas: 0.627 Water: 0.473	–	–

[a]For water flooding and WAG injection, the same model brine was used as for brine injection in the specific experiment

at 0.15 cm^3/min to mobilise S_{or_WF}. Afterwards, AS drive and N_2 were co-injected at a total injection rate of 1.1 cm^3/min (4.6 ft/day) to generate drive foam. Gas and liquid flowrates were adjusted to maintain a mid-core foam quality (i.e. gas fractional flow) of 57%. Continuous gas, WAG and ASF injection continued until no more measurable amounts of oil were produced.

Table 6 presents the physical properties of the various types of brine, oil, AS slug and AS drive solutions used in this work. In Exp. 4, water flooding was first done with 4.0 wt% NaCl brine. Afterwards, water salinity was reduced by extensively flooding the core with 2.0 wt% NaCl brine as a brine-slug salinity gradient was being avoided and the total ionic strength (TIS) of the AS slug corresponded to 2.0 wt% NaCl dissolved in demineralised water. In Exp. 5, 3.6 wt% NaCl brine, TIS equivalent to the AS slug formulation used, was injected immediately. This procedure ensured the absence of a brine–slug–drive salinity gradient. The core-floods are analysed in terms of (incremental) oil recovery, pressure data, CT scan images and corresponding saturation profiles.

2.5.4 CT Data Post-processing

As aforementioned, we only present CT scans for Exp. 4 and 5. The amount of dopant added to the oleic phase was reduced from 25 wt% (Exp. 4) to 20 wt% (Exp. 5) 1-iododecane as 25 wt% resulted in CT responses of oil in bulk (CT^B_{oil} in Table 7) that exceeded the default CT scale (− 1024 HU to 3072 HU). Consequently, for Exp. 4, the extended and hence less precise CT scale (− 10,000 HU to 30,000 HU) was used for determining CT^B_{oil}. In two-phase flow conditions, CT scan images were taken using one single energy beam of 140 kV while for defining three-phase saturation distributions scans were taken using simultaneously 140 kV and 80 kV energy beams. With the use of measured CT responses in HU, the formulae shown in Table 7 were applied to obtain porosity and saturation distributions (Sharma et al. 1997).

3 Results

3.1 IFT Measurements

The goal of the phase behaviour study conducted was to examine the n-hexadecane-AS slug phase behaviour at different salinities and to measure corresponding o/w IFTs at 90 °C. Figure 2 presents the measured o/w IFTs. IFTs between the selected AS slug and the model oil tend to decrease monotonically with increasing salinity (i.e. wt% NaCl). The lowest o/w IFT measured was $4.8 \pm 1.0 \times 10^{-2}$ mN/m and was found at a salinity of 2.0 ± 0.1 wt% NaCl. Although results do not indicate a distinct optimum salinity, optimum conditions are expected to be in the range of 2.0 ± 0.2 wt% NaCl or slightly higher than that. Indeed, for a similar o/w system, with the addition of 1.0 wt% Na_2CO_3 and 0.5 wt% AM IOS2024, Hosseini-Nasab and Zitha (2015) found optimum salinity conditions at nearly 2.6 ± 0.1 wt% NaCl. The addition of 1-iododecane, for CT contrast enhancement, to the oleic phase appears to reduce the o/w IFT slightly. It can be concluded that the surfactant concentration used in the AS slug (0.3 wt% AM IOS2024) was able to lower the o/w IFT with a factor of circa 130 and 540 for 0.4 wt% and 2.0 wt% NaCl samples, respectively. The ASF core-flood experiments performed in this study were done at under-optimum salinity conditions, o/w IFT of $1.9 \pm 0.2 \times 10^{-1}$ mN/m (0.4 wt% NaCl in Fig. 2), and at assumed (near-)optimum salinity conditions, o/w IFT of $4.8 \pm 1.0 \times 10^{-2}$ mN/m (2.0 wt% NaCl in Fig. 2).

Table 6 Physical properties of the types of brine, oil, AS slug and AS drive solutions used

	Experiment				
	1	2	3	4	5
Brine type	3.0 wt% NaCl	3.0 wt% NaCl 7.5 wt% KI[b]	3.0 wt% NaCl 15.0 wt% KI[b]	4.0 wt% NaCl 2.0 wt% NaCl	3.6 wt% NaCl
Brine density (g/cm^3)[a]	1.020 ± 0.001	1.078 ± 0.001	1.142 ± 0.001	1.027 ± 0.001 (4.0 wt%) 1.013 ± 0.001 (2.0 wt%)	1.024 ± 0.001
Brine viscosity (mPa s)[a]	1.07 ± 0.05	0.97 ± 0.08	1.01 ± 0.06	1.07 ± 0.05 (4.0 wt%) 1.03 ± 0.05 (2.0 wt%)	1.06 ± 0.06
Oil type	n-hexadecane < 0.006 wt% Oil Red O	n-hexadecane < 0.006 wt% Oil Red O 7.5 wt% 1-iododecane[b]	n-hexadecane < 0.006 wt% Oil Red O 5.0 wt% 1-iododecane[b]	n-hexadecane < 0.006 wt% Oil Red O 25.0 wt% 1-iododecane	n-hexadecane < 0.006 wt% Oil Red O 20.0 wt% 1-iododecane
Oil density (g/cm^3)[a]	0.775 ± 0.001	0.798 ± 0.001	0.790 ± 0.001	0.867 ± 0.001	0.841 ± 0.001
Oil viscosity (mPa s)[a]	3.37 ± 0.06	3.19 ± 0.06	3.22 ± 0.07	3.38 ± 0.03	3.31 ± 0.03
AS slug density (g/cm^3)[a]	–	–	–	1.013 ± 0.001	1.023 ± 0.001
AS slug viscosity (mPa s)[a]	–	–	–	1.07 ± 0.06	1.15 ± 0.05
AS drive density (g/cm^3)[a]	–	–	–	1.012 ± 0.001	1.023 ± 0.001
AS drive viscosity (mPa s)[a]	–	–	–	1.04 ± 0.05	1.10 ± 0.06

[a]All densities and viscosities mentioned were measured at 20 °C and atmospheric pressure
[b]Both the aqueous and oleic phases were doped. Corresponding CT data is not shown in this paper

Table 7 Equations used for post-processing CT scan data

	Formula
Porosity	$\phi = \frac{\mathrm{CT_{wet}} - \mathrm{CT_{dry}}}{\mathrm{CT_{brine}} - \mathrm{CT_{air}}}$
Two-phase oil saturation	$S_o = \frac{1}{\phi}\left(\frac{\mathrm{CT} - \mathrm{CT_{wet}}}{\mathrm{CT_{oil}} - \mathrm{CT_{brine}}}\right)$
Three-phase oil saturation	$S_o = \frac{(\mathrm{CT}^A - \mathrm{CT}^A{}_{\mathrm{wet}})(\mathrm{CT}^B{}_{\mathrm{dry}} - \mathrm{CT}^B{}_{\mathrm{wet}}) - (\mathrm{CT}^B - \mathrm{CT}^B{}_{\mathrm{wet}})(\mathrm{CT}^A{}_{\mathrm{dry}} - \mathrm{CT}^A{}_{\mathrm{wet}})}{\phi^A(\mathrm{CT}^A{}_{\mathrm{oil}} - \mathrm{CT}^A{}_{\mathrm{brine}})(\mathrm{CT}^B{}_{\mathrm{dry}} - \mathrm{CT}^B{}_{\mathrm{wet}}) - \phi^B(\mathrm{CT}^B{}_{\mathrm{oil}} - \mathrm{CT}^B{}_{\mathrm{brine}})(\mathrm{CT}^A{}_{\mathrm{dry}} - \mathrm{CT}^A{}_{\mathrm{wet}})}$
Three-phase gas saturation	$S_g = \frac{(CT^A - CT^A{}_{\mathrm{wet}})\phi^B(CT^B{}_{\mathrm{oil}} - CT^B{}_{\mathrm{brine}}) - (CT^B - CT^B{}_{\mathrm{wet}})\phi^A(CT^A{}_{\mathrm{oil}} - CT^A{}_{\mathrm{brine}})}{\phi^B(CT^B{}_{\mathrm{oil}} - CT^B{}_{\mathrm{brine}})(CT^A{}_{\mathrm{dry}} - CT^A{}_{\mathrm{wet}}) - \phi^A(CT^A{}_{\mathrm{oil}} - CT^A{}_{\mathrm{brine}})(CT^B{}_{\mathrm{dry}} - CT^B{}_{\mathrm{wet}})}$
Three-phase water saturation	$S_w = 1 - S_o - S_g$

CT_{dry}, CT_{wet}, CT_{air}, CT_{brine} and CT_{oil} stand for the CT response in HU of the dry core, brine saturated core, air phase, water phase and oil phase, respectively. Superscripts A and B relate to 140 kV and 80 kV CT data, respectively

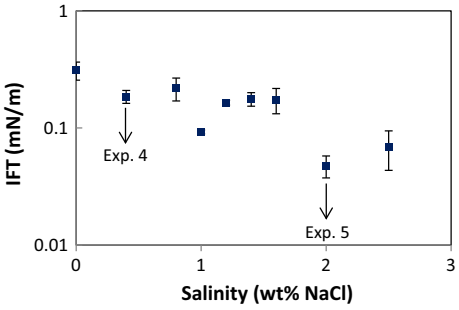

Fig. 2 IFT measurements conducted with a spinning-drop tensiometer. All systems consisted of X wt% NaCl, 1 wt% Na_2CO_3, 0.5 wt% sec-butanol and 0.3 wt% AM IOS2024 with n-hexadecane

3.2 Bulk Foam Stability

Bulk foam experiments were performed in the absence of oil to assess foaming capacity and foam stability in bulk for various AS drive solutions. Both salinity and surfactant concentration were varied. Results are shown in Fig. 3. It is found that increasing salinity has hardly any effect on foaming capacity, but reduces foam stability. Higher salt concentrations reduce the effective range of repulsive forces (i.e. Debye length), leading to earlier foam decay compared to lower salinities (Klitzing et al. 1999). An increase in surfactant concentration showed no significant effect on foaming capacity and foam longevity. Recall that both surfactant concentrations assessed (0.3 wt% and 0.6 wt% AM IOS2024) are well above its *c.m.c.* (3.0×10^{-3} wt% AM IOS2024). This implies that the surfactant adsorption density at the gas–water (g/w) interfaces barely changed upon varying surfactant concentration.

3.3 Core-Flood Experiments

A summary of the performed core-floods is presented in Table 8. The results of the preparatory part consisting of primary drainage (oil injection) and imbibition (water flooding) for Exp. 4 were described in detail elsewhere (Janssen et al. 2018) and are representative for all core-floods conducted. Only a brief summary of the preparatory injection stages is presented here. This paragraph continues with the following sections: primary drainage and forced imbibition, continuous N_2 and WAG injection, ASF: oil mobilisation and ASF: oil displacement by foam. Ultimate oil recoveries, oil (S_o) and gas (S_g) saturation profiles and pressure drops are analysed for each injection scheme.

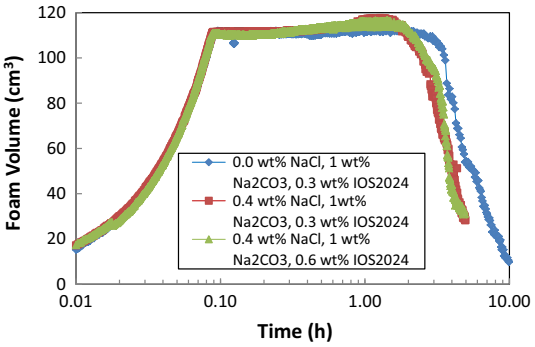

Fig. 3 Development of foam volumes at different salinities and surfactant concentrations at ambient temperature and atmospheric pressure. A foam half decay time ($t_{1/2}$) of 4.93 h was seen for the 0.0 wt% NaCl solution while both surfactant concentrations, in the presence of 0.4 wt% NaCl, showed half decay times of 3.70 h

Table 8 Summary of core-floods conducted

Exp.	k_{ro}*	k_{rw}*	S_{wc}	S_{oi}	S_{or_WF}	R_{FWF} (% of OIIP)	S_{or_EOR}	R_{FEOR} (% of OIIP)
1	0.48 ± 0.05	–	0.30 ± 0.02	0.70 ± 0.02	–	–	0.35 ± 0.02	50 ± 4
2	0.65 ± 0.07	0.14 ± 0.01	0.24 ± 0.02	0.76 ± 0.02	0.49 ± 0.02	36 ± 4	0.36 ± 0.02	53 ± 4
3	0.60 ± 0.05	–	0.26 ± 0.02	0.74 ± 0.02	–	–	0.30 ± 0.02	59 ± 4
4[a]	0.51 ± 0.02	0.13 ± 0.01	0.22 ± 0.04	0.78 ± 0.04	0.41 ± 0.02	47 ± 6	0.31 ± 0.03	60 ± 5
5[a]	0.66 ± 0.09	0.15 ± 0.01	0.17 ± 0.05	0.83 ± 0.05	0.41 ± 0.02	51 ± 7	0.21 ± 0.06	74 ± 8

k_{ro}*, k_{rw}*, S_{wc}, S_{oi}, S_{or_WF}, S_{or_EOR}, R_{FWF}, R_{FEOR} and OIIP represent the oil end-point relative permeability, water end-point relative permeability, connate water saturation, initial oil saturation, residual oil saturation to waterflood, residual oil saturation to N_2 flood/WAG/ASF, recovery factor corresponding to water flooding, recovery factor corresponding to N_2 flood/WAG/ASF and the oil initially in place, respectively

[a]Saturations and recovery factors shown are based on CT data post-processing

3.3.1 Primary Drainage and Forced Imbibition

During primary drainage, brine was displaced by oil in a distinctive frontal manner. In order to satisfy the zero capillary pressure condition at the outlet boundary, the wetting (i.e. aqueous) phase tends to accumulate near the core outlet (Huang and Honarpour 1998). Corresponding S_o profiles for Exp. 4 (Janssen et al. 2018) show a characteristic Buckley–Leverett displacement including a sharp shock front and a rarefaction wave upstream of it (Buckley and Leverett 1942). Constructed S_o profiles for water flooding in Exp. 4 revealed a less frontal displacement front compared to primary drainage due to more prominent capillary forces.

The derived oil and water end-point relative permeabilities, k_{ro}^* and k_{rw}^*, are in good agreement with the values reported earlier for similar water-wet sandstones (Treiber et al. 1972). Table 9 gives an overview of oil and water breakthrough times related to primary drainage and forced imbibition, respectively, for all core-floods conducted. The end-point mobility ratios (M) presented in Table 9 support the idea of a piston-like displacement of oil by water.

3.3.2 Continuous N_2 and WAG Injection

As mentioned before, the baseline core-floods were performed under gravity stable conditions (Table 5). This section continues with pressure drops and corresponding oil recovery profiles

Table 9 Overview of oil and water breakthrough times during primary drainage (PD) and water flooding (WF)

Exp.	Oil BT (PD)	Water BT (WF)	*M*
1	0.79 ± 0.02 PV	–	–
2	0.76 ± 0.02 PV	0.45 ± 0.02 PV	0.71 ± 0.24
3	0.78 ± 0.02 PV	–	–
4	0.75 ± 0.02 PV	0.37 ± 0.02 PV	0.84 ± 0.16
5	0.76 ± 0.02 PV	0.41 ± 0.02 PV	0.71 ± 0.23

The end-point mobility ratios (M) were calculated using the following formula: $(k_{rw*}/\mu_w)/(k_{ro*}/\mu_o)$ where μ_w and μ_o represent the water and oil viscosity, respectively

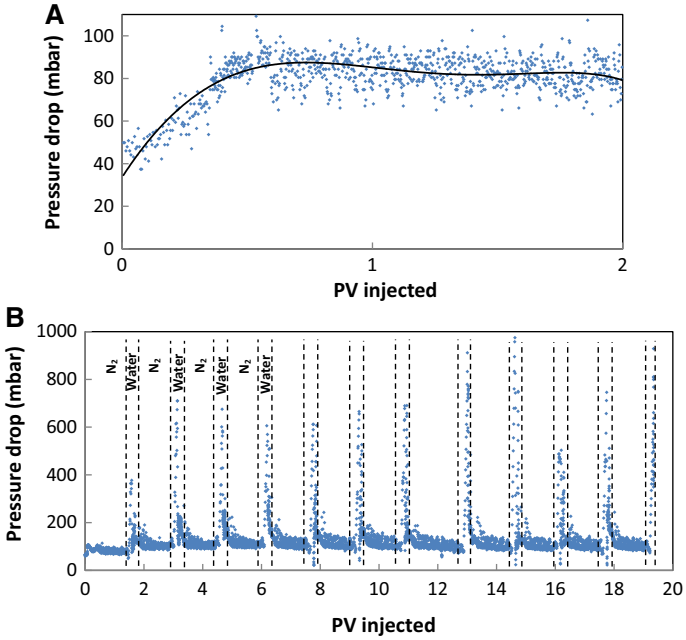

Fig. 4 Total pressure drop profiles during **a** N_2 flooding at S_{or_WF} (Exp. 2) and **b** WAG at S_{oi} (Exp. 3). A trend line (polynomial of the 5th order) is added to the data series shown in graph **a**. Note that for the first four WAG cycles the gas and water injection phases are shown

during N_2 flooding/WAG. Since the pressure drop profile for immiscible N_2 flooding at S_{oi} (Exp. 1) is similar to the one for Exp. 2, only the latter will be discussed in detail.

Figure 4 presents the total pressure drop profiles related to continuous N_2 injection at S_{or_WF} (Exp. 2) and WAG injection at S_{oi} (Exp. 3). In Exp. 2 gas was injected at 0.5 cm^3/min under gravity stable conditions (top-down) after the core was brought to S_{or_WF} (Fig. 4a). The estimated critical injection velocity was approximately 2.0 ft/day which equalled the gas injection rate (Dietz 1953). The gradually increasing trend in pressure drop during the first 0.45 ± 0.02 PV of injection reflects the downward propagation of the gas front. Here both water and oil were produced (Fig. 5). Gas breakthrough occurred at 0.51 ± 0.02 PV (similar to Exp. 1) after which pressure drops diminished slightly to 82 ± 7 millibar (mbar), pressure gradient of 0.48 ± 0.04 bar/m.

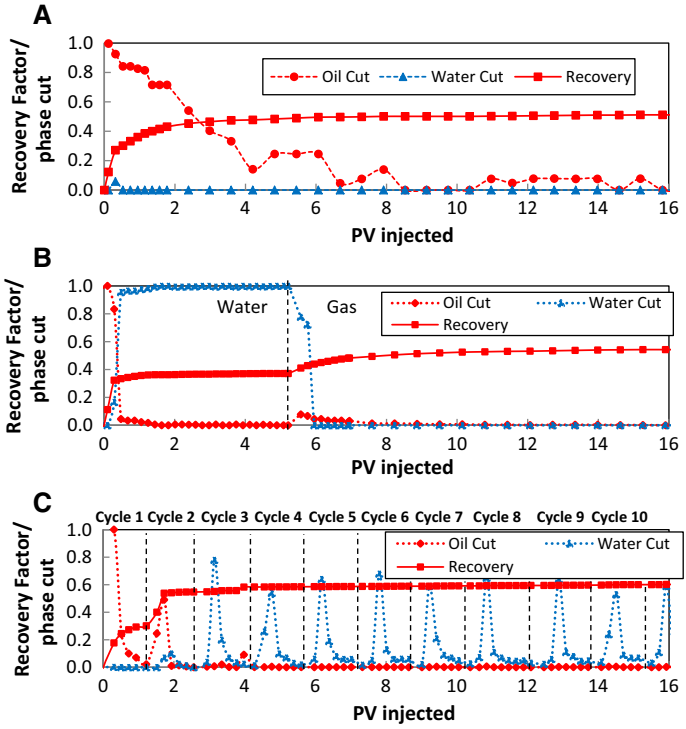

Fig. 5 Oil cut, water cut and recovery profiles for core-floods 1 (**a**), 2 (**b**) and 3 (**c**). Water, gas and cycle *X* refer to water flooding, gas flooding and injection of WAG cycle *X*. All values shown are with respect to the OIIP. Note that only the first 10 WAG cycles are presented

During WAG (Fig. 4b), gas and water were injected at 0.5 cm^3/min and 2.0 cm^3/min, respectively. Gas injection in the first WAG cycle shows a similar pressure drop profile compared to the one shown in Fig. 4a: an increase from 62 ± 2 to 103 ± 2 mbar followed by a slight decrease to 80 ± 5 mbar. Gas breakthrough occurred at 0.49 ± 0.02 PV. Subsequently, the shift from gas to water injection yielded a sharp increase in pressure drop to 363 ± 2 mbar. This is most probably due to a combination of the increased injection rate and the development of a trapped (i.e. non-movable) gas saturation (S_{gt}). It can be explained by considering Darcy's law for multi-phase flow in one dimension:

$$\Delta P = u_{tot}\left(\frac{f_o \mu_o}{k_{ro} k} + \frac{f_w \mu_w}{k_{rw} k} + \frac{f_g \mu_g}{k_{rg} k}\right) L \tag{3.1}$$

where ΔP, u_{tot}, μ_a, k_{ra}, k, f_a and L represent the pressure drop, total superficial velocity, viscosity of phase a, relative permeability of phase a, absolute permeability to brine, fractional flow of phase a and the core length, respectively. Subscripts *o*, *w* and *g* refer to the oil, water and gas phase, respectively. In order to satisfy the increase in pressure drop from 80 ± 5 to 363 ± 2 mbar, upon switching from gas to water injection, just an increase of u_{tot} by a factor 4 is not sufficient. This is due to the expected alterations in $\frac{\mu_o}{k_{ro} k}$ and $\frac{\mu_w}{k_{rw} k}$. As soon as water injection started, water (S_w) and oil (S_o) saturations, respectively, increased and decreased, implying an enlarged k_{rw} while k_{ro} most probably decreased only slightly due to a relatively small shift in S_o. The above entails that the reduction of $\frac{\mu_w}{k_{rw} k}$ was of a larger magnitude

than the increase of $\frac{\mu_o}{k_{ro}k}$, suggesting that $\frac{\mu_g}{k_{rg}k}$ needed to be enlarged to satisfy the observed increase in pressure drop when shifting from gas to water injection in the first WAG cycle. It required a reduction of k_{rg} due to lowering of the free (i.e. flowing) gas saturation (S_{gf}) by production of gas and the formation of S_{gt}.

During injection of the second gas slug, the total pressure drop decreased to a steady state value of 102 ± 10 mbar; pressure gradient of 0.60 ± 0.06 bar/m. The higher pressure drop for gas injection, compared to the first WAG cycle, is most likely due to the presence of S_{gt} in combination with the introduced water phase in the previous cycle. Water injection at the end of the second cycle resulted in a peak pressure drop of 709 ± 2 mbar. The relatively high pressure drops during water injection in all succeeding WAG cycles are consistent with earlier work of Dong et al. (2005). Most likely S_{gf} decreased, whereas S_{gt} increased, yielding reduced k_{rg}. The increment in S_{gt} can furthermore restrict water flow through the pores, reducing k_{rw}.

Figure 5 shows the oil cut, water cut and oil recovery profiles for Exp. 1, 2 and 3. The recovery profile for Exp. 1 shows that roughly half of the ultimate oil recovery was achieved before gas breakthrough occurred. Eventually, after 16 PV of gas injected, a final recovery factor of $50 \pm 4\%$ of the oil initially in place (OIIP) was reached (R_{FEOR} in Table 8). During water flooding in Exp. 2 bulk of the oil was produced prior to water breakthrough (0.45 ± 0.02 PV). After water breakthrough occurred, limited amounts of oil were produced, increasing the recovery factor (R_{FWF} in Table 8) from 31 ± 4 to $36 \pm 4\%$ of the OIIP. The relatively low R_{FWF} might be affected by the low absolute permeability of the core used; smaller pore sizes yield higher capillary forces that may keep the oil in place. Including immiscible gas flooding, the ultimate R_F reached $53 \pm 4\%$ of the OIIP (R_{FEOR} in Table 8), which implies an incremental oil recovery of $17 \pm 8\%$ of the OIIP. However, it should be noticed that the incremental recovery might be an overestimation due to the suspected low R_{FWF}. Oil swelling and oil viscosity reduction are negligible displacement mechanisms during immiscible gas injection (Exp. 1 and 2), since the system operated well below the expected MMP of roughly 350 bar (Sebastian and Lawrence 1992).

During WAG injection at S_{oi} (Exp. 3), in the first cycle, only oil was produced until gas breakthrough occurred. The plot clearly shows that most of the oil was being produced throughout the first two WAG cycles ($R_{Fcycle2}$ equalled $53 \pm 4\%$ of the OIIP). This can be explained by a good contact between the oil in place (OIP) and the injected phases. Finally, after successfully injecting 12 WAG cycles, a R_{FEOR} of $59 \pm 4\%$ of the OIIP was reached; equivalent to a residual oil saturation to WAG (S_{or_EOR} in Table 8) of 0.30 ± 0.02.

3.3.3 ASF: Oil Mobilisation

In Exp. 4 and 5, an AS slug was injected into the previously water-flooded cores to attempt the mobilisation of S_{or_WF}, at under-optimum and (near-)optimum salinity conditions, respectively (Fig. 2). The resulting pressure drops are shown in Fig. 6. As soon as the AS slug contacted the core in Exp. 4, the pressure drop increased sharply from 59 ± 7 to 83 ± 7 mbar at 0.07 ± 0.02 PV injected. Thereafter, pressure drop continued to increase reaching 97 ± 7 mbar at the end of slug injection. The increase in pressure drop is due to the formation and propagation of the oil bank (Janssen et al. 2018). The slope of the pressure drop versus PV injected decreased over time due to the modification of the oil bank. The pressure drop profile corresponding to Exp. 5 shows an increase from 59 ± 7 to 73 ± 7 mbar at 0.09 ± 0.02 PV injected and afterwards it slightly reduced.

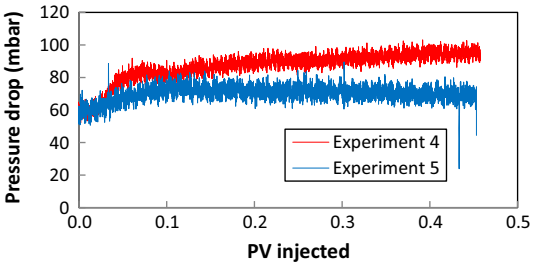

Fig. 6 Total pressure drop profiles during AS slug injection in experiments 4 and 5. A total of 0.46 ± 0.02 PV AS slug was injected using an injection rate of 0.15 cm^3/min (0.62 ft/day)

The CT images and S_o profiles for Exp. 4 and 5 are presented in Fig. 7. It is evident that a sharp oil bank, with peak S_o of 0.64 ± 0.02 and 0.69 ± 0.02 for Exp. 4 and 5, respectively, was formed after 0.06 PV (Exp. 4) and 0.07 PV (Exp. 5) injected. For further analysis, first Exp. 4 will be discussed. As injection continued, the oil bank became more dispersed as indicated by the gradual reduction of S_o on the leading edge (downstream side). Yet, peak S_o remained fairly constant around 0.67 ± 0.02; suggesting average water saturations (S_w) slightly higher than S_{wc} within this part of the oil bank (Table 8). Due to an expected non-optimal sweep efficiency, i.e. unfavourable AS slug–oil mobility ratio, the upstream area of the core was not perfectly swept and various oil remnants can be seen. Finally, after 0.46 PV AS slug injection, an averaged S_o of 0.33 ± 0.04 was observed upstream of the oil bank. The leading edge propagated with a velocity slightly higher than the trailing edge, i.e. upstream side (128 ± 5 cm/PV vs. 92 ± 5 cm/PV); implying a continuously growing oil bank.

The oil bank formation in Exp. 5 reflects the fact that the AS slug was at (near)-optimum salinity conditions. The oil bank is characterised by a more uniform S_o distribution. Due to a roughly four times lower o/w IFT compared to Exp. 4 (see Sect. 3.1), mobilisation of S_{or_WF} improved hence increasing the amount of oil that was available for oil coalescence. Most likely this caused a greatly diminished dispersion effect on the leading edge as well as a more extended oil bank (compared to Exp. 4). Furthermore, lower values for peak S_o were seen (0.60 ± 0.02). The latter might be a result of reduced capillary forces, that kept the oil trapped, when flooding at (near-)optimum slug salinity. Decreased capillary forces yield lower amounts of residual oil, reducing that part of peak S_o that is immobile. At the end of AS slug injection, the averaged S_o upstream of the oil bank equalled 0.10 ± 0.02. Lower estimated propagation velocities were found for the leading edge (93 ± 5 cm/PV) and the trailing edge (61 ± 5 cm/PV) compared to Exp. 4, suggesting an increase in the oil bank's expansion rate. It is evident from the CT scans shown in Fig. 7 that oil coalescence was substantial at the leading edge. It remains inconclusive how the o/w IFT lowering affects the coalescence of oil. Previous studies suggested that the rate of oil coalescence appears to be a function of interfacial viscosity rather than IFT, with lower interfacial viscosities promoting oil coalescence (Wasan et al. 1978; Fayers 1981; Aderangi and Wasam 1995).

The relationship between the shape of the oil bank and related pressure drop was studied for a test case and is presented in "Appendix A". The biggest contribution to the pressure drop comes most likely from the relatively high S_o within the oil bank. At those locations, pressure drop significantly increased due to a substantial lowering of the water mobility $\left(\lambda_w = \frac{k_{rw}k}{\mu_w}\right)$. It is most probably for this reason that Exp. 4 revealed higher pressure drop values over the course of AS slug injection than Exp. 5 (Fig. 6). The initial, relatively sharp, increasing trend in pressure drop during both Exp. 4 and 5 reflects the formation of a sharp oil bank. Subsequently, in Exp. 4, the more gradually increasing pressure drop (Fig. 6) matches the continuously expansion of the oil bank while maintaining, or slightly increasing, its peak S_o.

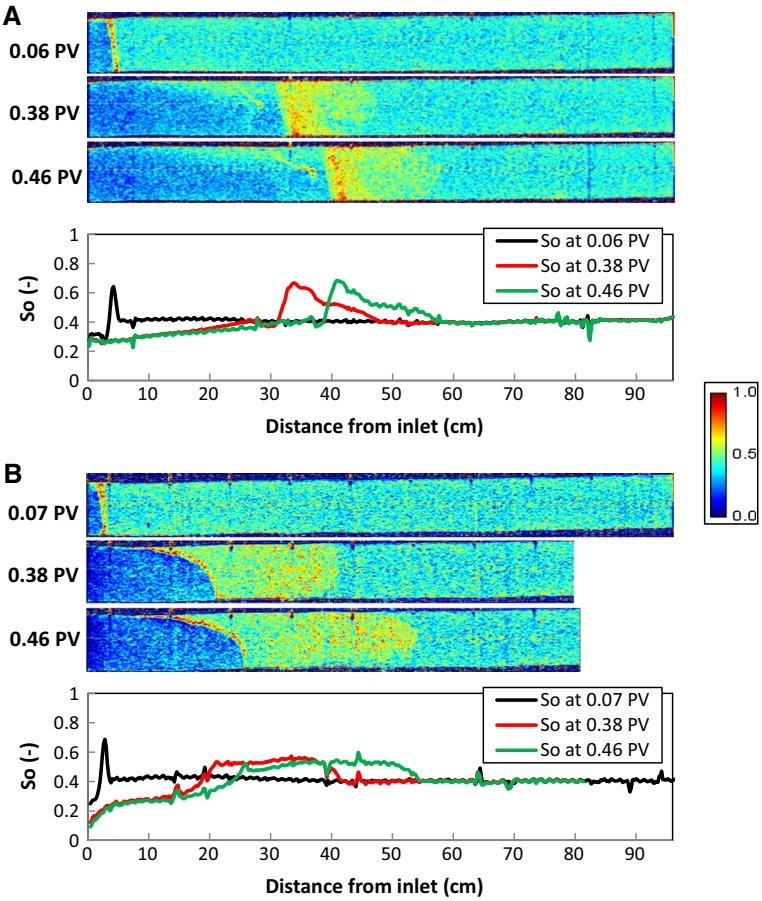

Fig. 7 Oil saturation CT scan images and corresponding saturation profiles during AS slug injection for Exp. 4 (**a**) and Exp. 5 (**b**). Note that the last two scans taken during Exp. 5 do not include the full outlet section as S_o was not altered there ($S_o = S_{or\_WF}$). The images shown have X:Y ratios of 3:1. Red refers to oil and blue indicates water

In Exp. 5, after the initial increase, total pressure drop reduced slightly due to a combination of the reduction in peak S_o (decreasing pressure drop) and the expansion of the oil bank (increasing pressure drop).

CT images taken during both experiments reveal gravity underriding effects of the injected aqueous AS slug. This effect seems to be more strongly present in Exp. 5. The end-point dimensionless gravity number (N_g), calculated using Eq. 3.2, characterises the ratio of gravitational to viscous forces. The more obvious gravity underriding effect in Exp. 5 (N_g of 0.56) compared to Exp. 4 (N_g of 0.31) is mainly due to the effective density difference at the trailing edge's interface. The end-point dimensionless gravity number is calculated as follows (Hagoort 1980):

$$N_g = \frac{k k_{ro}{}^* \Delta\rho_{wo} g}{\mu_o u_t} \tag{3.2}$$

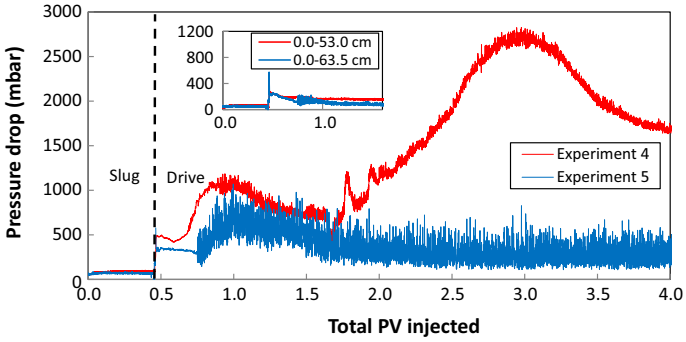

Fig. 8 Total pressure drop profiles during AS slug injection and AS drive co-injection for Exp. 4 and 5. Co-injection of AS drive solution with N_2 took place at a total injection rate of 1.10 cm^3/min (4.58 ft/day). The upper left graph presents the pressure drop over, respectively, the first 53.0 cm (Exp. 4) and 63.5 cm (Exp. 5). Due to failure of the liquid pump only gas was injected between 1.68 ± 0.02 and 1.72 ± 0.02 PV in Exp. 4. Hence, for the analysis we only consider injection times prior to 1.68 ± 0.02 PV

where k, k^*_{ro}, $\Delta\rho_{wo}$, g, μ_o and u_t represent the absolute horizontal permeability to brine, end-point relative permeability of the oil, density difference between the injected slug and the displaced oil, gravitational acceleration, viscosity of the oleic phase and the total volumetric Darcy velocity, respectively.

3.3.4 ASF: Oil Displacement by Foam

Following AS slug injection for oil mobilisation, AS drive formulations (Table 4) were co-injected with N_2 at a foam quality of 57%. Figure 8 shows corresponding total pressure drop profiles related to AS slug and drive co-injection. This section only focuses on the AS drive co-injection phase. Let us again first consider Exp. 4. The complete pressure drop profile is the result of a combination between displacing the oil bank and foam generation. As soon as co-injection was initiated, a steep increase in pressure drop to 485 ± 3 mbar was observed due to the increase in total flowrate. Afterwards, pressure drop slightly decreased to 422 ± 2 mbar at 0.59 ± 0.02 PV (PV refers to the sum of gas and liquid PV injected, i.e. total PV). The reduction in pressure drop most likely indicates a decrease of the oil bank's peak S_o (see "Appendix A" and Sect. 3.3.3 for the effect of high S_o on pressure drop). From 0.59 ± 0.02 PV onwards, the total pressure drop increased until it reached a maximum of 1040 ± 61 mbar at 0.95 ± 0.02 PV. Afterwards, it slightly decreased to 702 ± 34 mbar corresponding to an averaged pressure gradient of 1.25 ± 0.08 bar/m. The latter behaviour of the pressure drop is expected to be due to weak foam generation downstream (note the constant low pressure drop in the first 53.0 cm). Due to failure of the liquid pump, only gas was injected from 1.68 ± 0.02 to 1.72 ± 0.02 PV. Afterwards, co-injection continued with a gas fractional flow of 57%. As a result of this, a new foam front was developed indicated by the steep increase in total pressure drop from 1.80 ± 0.02 to 2.90 ± 0.02 PV. Hence, for further analysis in this paper, we only focus on injection times prior to the liquid pump failure in Exp. 4. Production of the oil bank started at 0.65 ± 0.02 PV and foam breakthrough occurred at 0.86 ± 0.02 PV (0.40 ± 0.02 PV since co-injection started).

During AS drive and N_2 co-injection in Exp. 5, again a steep increase in pressure drop was observed due to the change in total flowrate. The sharp increase yields lower pressure drop values compared to Exp. 4 mainly due to the difference in saturation distribution. The oil

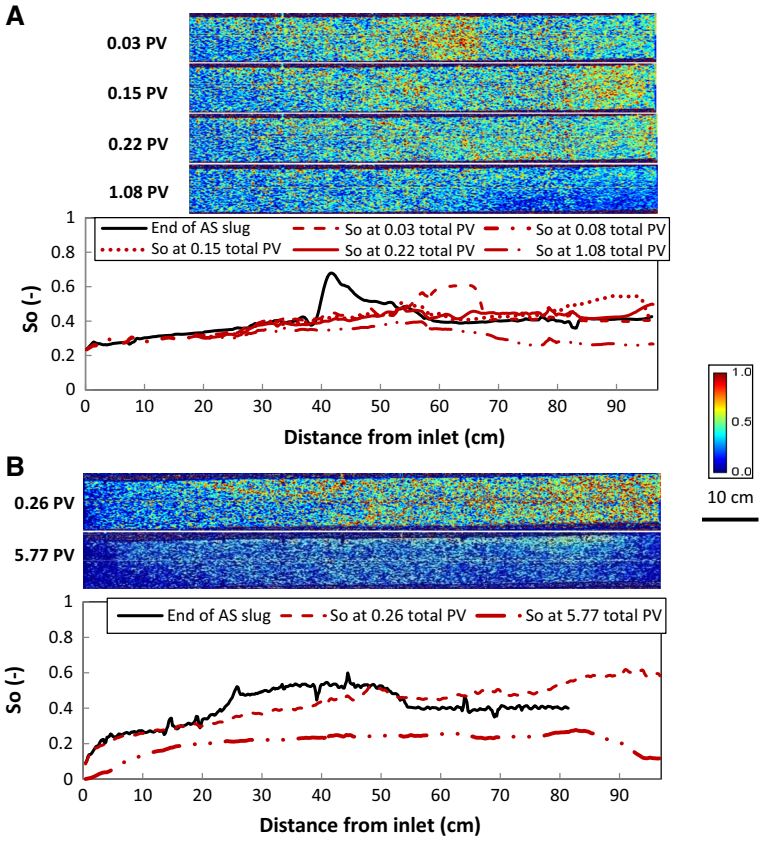

Fig. 9 Oil saturation CT scan images and corresponding saturation profiles during foam drive co-injection for Exp. 4 (**a**) and Exp. 5 (**b**). PV = 0 corresponds to the start of the co-injection. Note that in Exp. 4 only the last 79 cm of the core could be scanned due to CT limitations; a separate scan of the inlet was taken at 0.08 PV. The presented profiles were constructed by applying a moving average function with an interval of 6 to the processed data

bank formed in Exp. 5 exhibits a more uniform S_o distribution, with relatively low peak S_o. The reduction in peak S_o (compared to Exp. 4) most probably implies a substantial increase in water mobility, whereas oil mobility reduced slightly, resulting in a reduced pressure drop. Subsequent to the sharp increase, a slight reduction in pressure drop to 297 ± 9 mbar at 0.74 ± 0.02 PV was seen. Afterwards, the pressure drop increased before starting to decline again to reach a steady state pressure drop of 303 ± 103 mbar; averaged pressure gradient of 0.66 ± 0.31 bar/m. Similar to the previously discussed Exp. 4, this behaviour in pressure drop (i.e. increasing pressure drop followed by a slight decrease) is believed to be related to weak foam generation downstream, as low pressure drops were observed in the first 63.5 cm. Oil bank breakthrough occurred at 0.71 ± 0.02 PV, causing the total pressure drop to fluctuate. Foam breakthrough was observed at 0.90 ± 0.02 PV (0.44 ± 0.02 PV since co-injection started).

Figure 9 presents CT images and S_o profiles related to the foam drive in Exp. 4 and 5. First the images and profiles related to Exp. 4 will be considered. As soon as co-injection started the shape of the oil bank changed. Peak saturations were reduced, leading to a more uniform oil

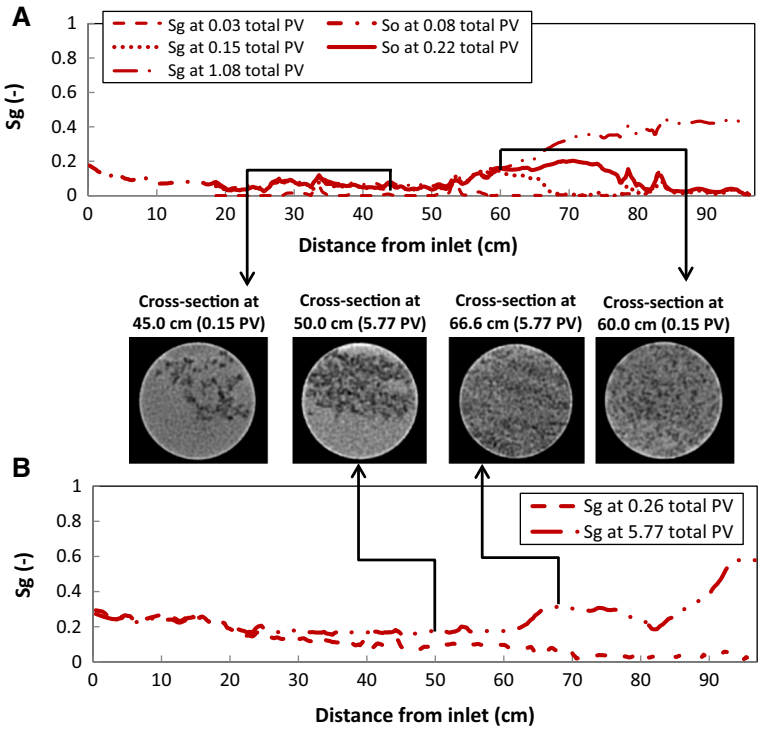

Fig. 10 Gas saturation profiles during foam drive co-injection in Exp. 4 (**a**) and Exp. 5 (**b**). Note that in Exp. 4 only the last 79 cm of the core could be scanned due to CT limitations; a separate scan of the inlet was taken at 0.08 PV. The presented profiles were constructed by applying a moving average function with an interval of 6 to the processed data. The cross-sectional areas shown represent the original CT data in Hounsfield units where the gas phase is represented in black

bank. Its breakthrough occurred after 0.19 ± 0.02 PV of co-injection. After 1.08 PV injected the complete oil bank was produced, yielding a S_{or_EOR} of 0.31 ± 0.03. It is clear from the CT images that mainly the downstream area of the core was swept.

The CT scan taken after 0.26 PV injected during Exp. 5 shows the situation just after oil bank breakthrough (occurred after 0.25 ± 0.02 PV co-injection). The later oil bank breakthrough at (near-)optimum salinity compared to under-optimum salinity is expected to be due to the difference in accessible pore volume. As at (near-)optimum salinity, more residual oil was mobilised and thus available for oil coalescence, and consequently, more pores were accessible for the oil bank to propagate through. Finally, after 5.77 PV of injection, no more oil was produced, and a S_{or_EOR} of 0.21 ± 0.06 was reached. In contrast to flooding at under-optimum salinity conditions, here the entire core was equally swept.

Figure 10 shows the S_g profiles during co-injection of AS drive solution and N_2 to form a foam drive for both Exp. 4 and 5. The constructed profiles for Exp. 4 show a clear trend where S_g remained rather low until a distance of 50 ± 1 cm. From that point onwards, S_g increased which is a qualitative indicator of foam generation (i.e. gas phase starts to divide equally across the rock's cross-sectional area; note the cross sections shown in Fig. 10a). In the first 50 ± 1 cm, gas override occurred, as illustrated by the cross section shown at 45.0 cm at 0.15 PV injected. The coarse, partly overriding, gas bubble distribution changed to a more equally

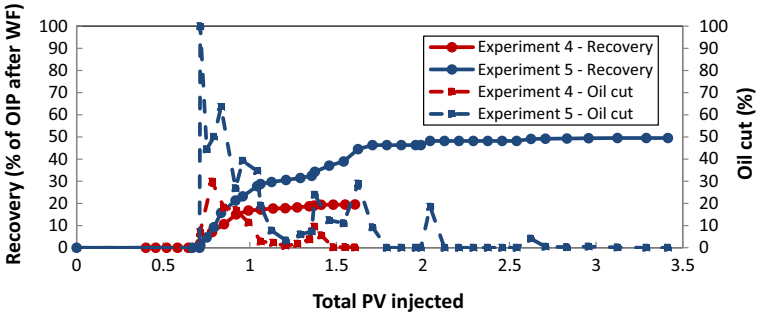

Fig. 11 Oil cut and cumulative recovery for experiments 4 (red) and 5 (blue). The recovery uses the oil in place after water flooding as a reference. PV = 0 corresponds with the start of AS slug injection; drive foam co-injection started at 0.46 PV. The profiles were constructed from material balance calculations. Note that for Exp. 4 only the data prior to the liquid pump failure (Fig. 8) are shown

divided gas bubble distribution as demonstrated by the cross section presented at 60.0 cm (0.15 PV injected). The foam front propagated with an average velocity of 144 ± 5 cm/PV, and its breakthrough was observed at 0.40 ± 0.02 PV.

The S_g profiles corresponding to Exp. 5 reveal the same general trend: fairly low saturations before reaching a distance of 62 ± 1 cm where S_g started to increase. Again, as depicted by the two cross-sectional areas shown in Fig. 10b, gas was partly overriding upstream of 62 ± 1 cm whereas a more uniform gas distribution was observed downstream. The averaged velocity of the foam front was 156 ± 5 cm/PV and its breakthrough occurred at 0.44 ± 0.02 PV. It remains unclear why gas seems to accumulate near the core outlet.

3.3.5 ASF: Oil Recovery

Cumulative oil recovery and oil cut plots for both ASF experiments are shown in Fig. 11. First 0.46 PV of AS slug was injected which did not produce any measurable amounts of oil. In both core-flood experiments performed, oil bank breakthrough occurred at similar times. Once breakthrough happened in Exp. 4, the oil cut increased progressively until it reached a peak value of $30 \pm 5\%$ at 0.78 ± 0.02 PV. Afterwards, it slightly reduced to zero. Clean oil production by the oil bank continued until a micro-emulsion broke through at 1.24 ± 0.02 PV. Its production lasted till 1.41 ± 0.02 PV. Eventually, after 1.63 ± 0.02 PV, the produced clean oil–emulsified oil ratio equalled approximately 10 and the oil recovery reached $20 \pm 3\%$ of the OIP after WF (equivalent to a R_{FEOR} of 60 ± 5 of the OIIP; Table 8).

Higher oil cuts were obtained for Exp. 5 [(near-)optimum salinity] after breakthrough of the oil bank compared to Exp. 4 (under-optimum salinity) due to a larger volume of the continuous mobilised oil phase within the oil bank. Its profile is very similar to the one corresponding to Exp. 4: a sharp increase in oil cut followed by a more gradually decreasing trend. It implies diffusive behaviour of the trailing edge of the oil bank. Whereas in Exp. 4, it only took 1.24 ± 0.02 PV for the oil bank to be completely produced, here clean oil production by the oil bank went on until 2.62 ± 0.02 PV injected. Afterwards, very little amounts of micro-emulsions were produced, yielding a clean oil–emulsified oil ratio of roughly 106 in the effluents. Finally, after 3.41 ± 0.02 PV, an oil recovery of $50 \pm 7\%$ of the OIP after WF was achieved; R_{FEOR} of 74 ± 8 of the OIIP (Table 8). In both experiments the rate of oil recovery was greatly diminished as soon as foam breakthrough occurred.

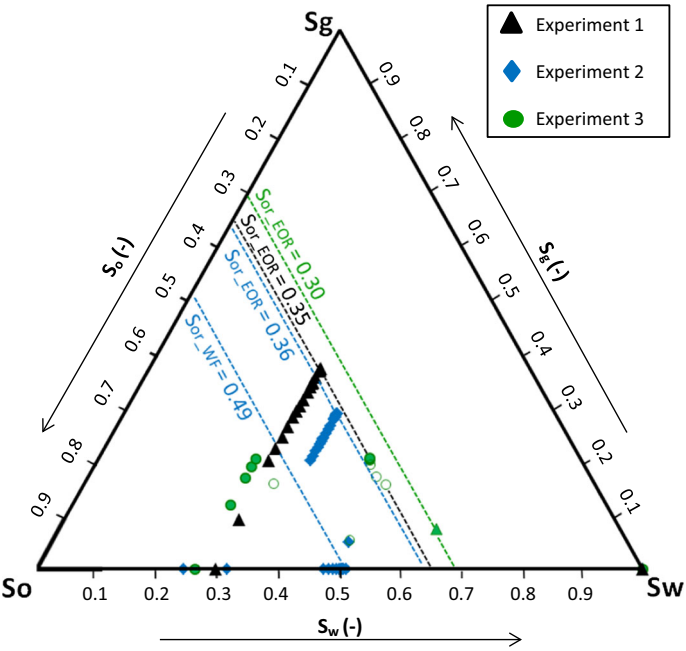

Fig. 12 Saturation paths for Exp. 1, Exp. 2 and Exp. 3. S_w, S_o, S_g, S_{or_WF} and S_{or_EOR} represent the water, oil, gas, residual oil to waterflood and residual oil to immiscible gas/WAG, respectively. Three-phase saturations shown were averaged over the entire core and calculated using material balance calculations. The closed and open circles in Exp. 3 represent the gas and water injection during the first two WAG cycles, respectively. The green triangle indicates the saturation distribution after successfully injecting 12 full WAG cycles

4 General Discussion

In the discussion, we will elaborate on the results presented in this paper in the light of mobilisation and displacement mechanisms. The evolutions of three-phase saturations during the course of gas flooding, WAG and ASF are displayed in ternary saturation diagrams. The diagrams provide a schematic way of comparison between various saturation paths, allowing us to develop mechanistic conceptual models for oil displacement. Furthermore, conceptual models are suggested for the development of the oil bank (oil mobilisation mechanism) and its displacement by foam (foaming mechanism) during ASF.

4.1 Saturation Paths: Gas Flooding and WAG

Saturation paths were constructed for Exp. 1, 2 and 3 using material balance calculations at fixed time intervals, as shown in Fig. 12. In Exp. 1 N_2 injection took place at an essentially constant S_{wc}, indicating effectively two-phase gas-oil flow where the propagating gas front displaced the oil towards the outlet. Film flow, i.e. oil drainage from the pores and subsequently oil spreading across the gas–water interface, might be an additional displacement mechanism responsible for the oil recovery in Exp. 1 after the advanced gas–oil interface reached the core outlet (Oren et al. 1992; Vizika 1993; Blunt et al. 1995; Khorshidan et al. 2016). Film flow requires a capillary pressure sufficiently high for gas to enter a pore throat and the oil spreading coefficient should exceed a critical value as well.

In Exp. 2, water flooding was applied prior to N_2 injection. The injection of N_2 reveals oil displacement that follows a saturation path consisting of two segments. At first, the displacement of oil follows a path of roughly constant S_o, and here mainly water was produced. Afterwards, a similar saturation path can be observed as in Exp. 1: gas displacing the oil at a constant S_w slightly higher than S_{wc} (indicating two-phase gas-oil flow). The fairly high incremental oil recovered by N_2 flooding over water flooding might be influenced by the idea that water flooding did not reach true S_{or_WF} but a somewhat higher saturation.

The saturation path related to Exp. 3 supports the concept that S_{or_EOR} obtained by gas flooding is lower under three-phase flow conditions compared to two-phase flow conditions. The newly introduced gas, non-wetting, phase may start to occupy larger pores in the system. It might push out part of the previously present oil globules, which is now the intermediate-wetting phase, that could finally be transported by the injected water and gas (Shandrygin et al. 2015). Its saturation path also show that the bulk of the oil was produced during the first two WAG cycles, reaching a recovery similar to the ultimate oil recovery in Exp. 1 and 2 ($R_{Fcycle2}$ equalled $53 \pm 4\%$ of the OIIP). However, the amount of gas required to reach this recovery was greatly reduced compared to Exp. 1 and 2. S_{gt} increased drastically during water injection in those first two cycles, resulting in a lower gas relative permeability and consequently lower gas mobility. Lower gas mobility favours mobility control when gas is displacing oil. The latter most likely accounts for the relatively high R_{FEOR} observed in Exp. 3. These findings are in good agreement with previous studies of others (Zhang et al. 2010; Fatemi and Sohrabi 2013).

4.2 Saturation Paths: ASF

Figure 13 presents the sectional saturation paths for the two ASF core-flood experiments (Exp. 4 and 5) reported in Sects. 3.3.3 and 3.3.4. Averaged three-phase saturations were calculated using acquired CT slices at, respectively, 40 and 75 cm distance from the inlet. Those specific locations were selected as they represent the area prior and after the jump in S_g (Fig. 10). Let us first consider the diagrams (40 cm vs. 75 cm) corresponding to under-optimum salinity ASF (Exp. 4). As primary drainage and water flooding yielded uniform saturation distributions, the main difference between the two locations in space was seen during AS slug and AS drive co-injection. The formed oil bank by AS slug injection finally propagated to a distance of approximately 40–60 cm from the inlet, yielding increased S_o at 40 cm distance while no saturation alterations were observed at a distance of 75 cm. During co-injection of AS drive solution and N_2 (at 40 cm distance), first water was displacing the oil bank, reducing S_o. Subsequently, the co-injected N_2 with surfactant solution reduced S_w at a constant S_o before displacing a relatively small amount of oil in a way where S_w and S_g increased evenly. Most likely, the small amount of oil displaced is due to a lack of drive mobility control as foam was not generated yet (Fig. 10a). At 75 cm distance from the inlet, foam was generated, hence the increase in S_g. During drive co-injection, at first S_o slightly increased due to the propagation of the oil bank. Afterwards, similar to its saturation path at 40 cm distance, S_o remained constant, whereas S_w diminished and S_g increased (0.22 total PV), suggesting water displacement by foam at this point. Finally, oil was being produced by the foam front at a constant S_w. Eventually, S_{or_EOR} was lower at 75 cm distance compared to 40 cm distance from the inlet due to better mobility control.

The sectional saturation paths constructed for Exp. 5 show similar primary drainage and water flooding behaviour as Exp. 4. AS slug injection resulted in an increase in S_o only at a distance of 40 cm due to the position of the oil bank at the end of the injection phase (Fig. 7).

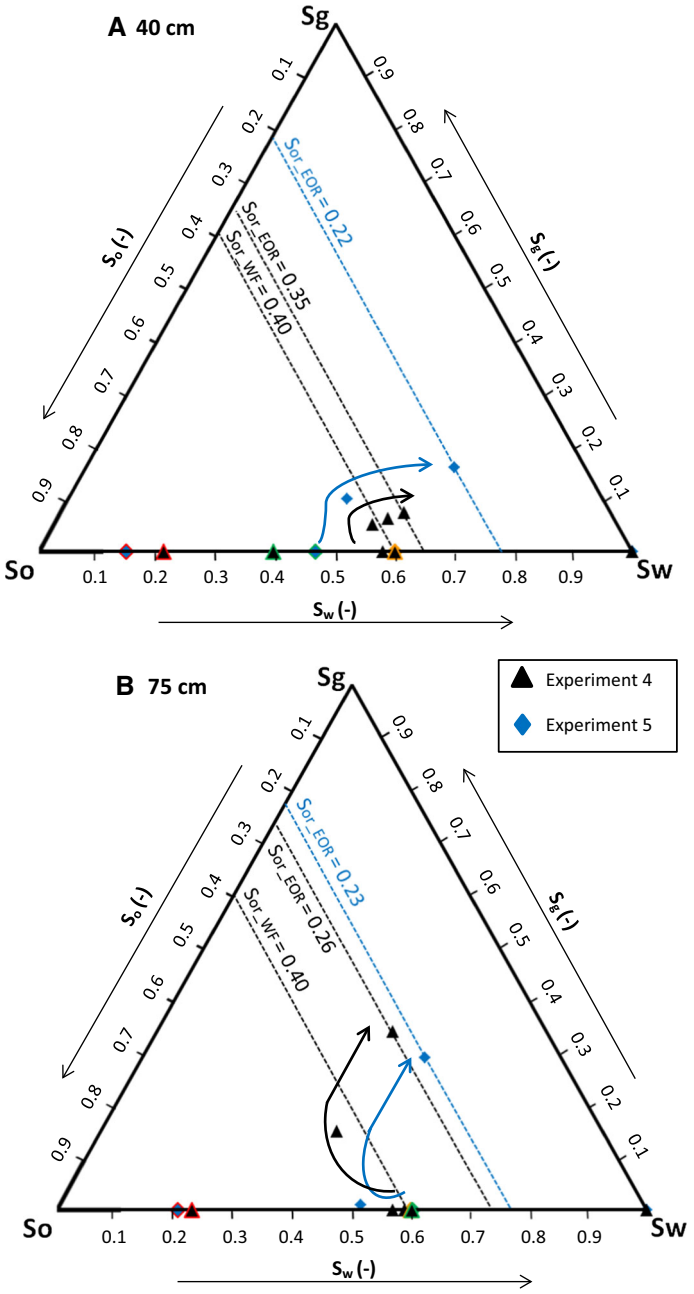

Fig. 13 Sectional saturation paths constructed for Exp. 4 (black triangles) and Exp. 5 (blue diamonds) at a distance of 40 cm (**a**) and 75 cm (**b**) from the inlet. S_w, S_o, S_g, S_{or_WF} and S_{or_EOR} represent the water, oil, gas, residual oil to waterflood and residual oil to chemical EOR saturations, respectively. Three-phase saturations shown were averaged and calculated using CT data. The data points outlined in red, orange and green represent the initial oil saturation, residual oil to waterflood and the condition at the end of AS slug injection, respectively

Note that S_o at the end of AS slug injection at 40 cm distance is lower compared to Exp. 4 due to the presence of a more uniform oil bank with lower peak S_o (Sect. 3.3.3). Oil was displaced by the co-injected N_2 and surfactant solution at 40 cm distance (after 0.26 total PV), while at 75 cm distance, oil was replacing water as the oil bank propagated downstream. Afterwards, at 40 cm distance, a similar saturation path compared to Exp. 4 was seen (i.e. displacement of oil where S_w and S_g increased equally). However, lower S_{or_EOR} was reached due to flooding at (near-)optimum salinity ($S_{or\_EOR} = 0.23$ vs. 0.35). The diagram corresponding to a distance of 75 cm from the inlet shows similar features as the saturation path related to Exp. 4 at the same distance. Although only two data points are available here (due to the amount of CT scans taken), they suggest oil displacement by drive foam at a nearly constant S_w as well. Note that the final S_{or_EOR} at 75 cm distance for Exp. 5 (0.23) is very similar to the one observed for Exp. 4 (0.26).

4.3 Saturation Paths: Gas Flooding and WAG Versus ASF

Saturations paths for Exp. 1 and 2 (Fig. 12) reveal similarities with saturation paths corresponding to oil being displaced by a stable drive foam in Exp. 4 and 5 (Fig. 13b): the displacement of oil at a nearly constant S_w. However, due to the combining effect of lower o/w IFTs and more favourable mobility control, ASF was able to mobilise and displace significant more oil than continuous N_2 injection. WAG showed a distinctive saturation path. It indicated that, when applying WAG for gas mobility control, S_{or_WF} (Exp. 2) and S_{or_EOR} (Exp. 1 and 2) could easily be reached after injecting the first and second WAG cycle, respectively. Although the oil recoveries by WAG and under-optimum ASF are very similar, ASF flooding at (near-)optimum salinity was able to enhance the oil recovery with approximately 15% of the OIIP with respect to WAG.

4.4 Development of the Oil Bank: Mobilisation Mechanism

Let us turn now to the AS slug injection in Exp. 4 and 5 and attempt to develop a conceptual model for the formation of the oil bank. Figure 14 presents a schematic representation of the proposed mobilisation mechanism. It includes entrapping of oil ganglia (i.e. clusters of connected oil droplets) due to capillary forces, o/w IFT lowering, mobilising oil ganglia and solubilising remaining residual oil. It is believed that S_{or_WF} involved mainly oil ganglia trapped within the pore structure due to capillary forces (Howe et al. 2015). During AS slug injection, the o/w IFT was reduced by approximately a factor of 130 (under-optimum) or 540 [(near-)optimum]. Consequently, the capillary number (10^{-7} after water flooding) increased proportionally, resulting in oil ganglia being mobilised and allowing them to propagate through narrow pore throats. The mobilised ganglia might break up and form sub-pore size oil droplets, as reported in previous studies (El Din Saad Ibrahim 2009). Mobilised ganglia and sub-pore size oil droplets may tend to coalesce to form an oil bank. During its propagation, oil coalescence occurred at the leading edge, promoting expansion of the oil bank, whereas oil entrapment might occur at its trailing edge by snap-off, yielding residual oil. It is likely that the residual oil to AS slug (S_{or_AS}) involved primarily sub-pore size oil droplets rather than oil ganglia.

The propagation of the oil bank through the porous medium causes dispersion of surfactant solution, oil and brine. At the trailing edge, i.e. oil bank/AS slug front, oil droplets were solubilised forming a micro-emulsion. The key reason for producing significantly more clean oil than solubilised oil when flooding at (near-)optimum conditions is that due to the lower o/w

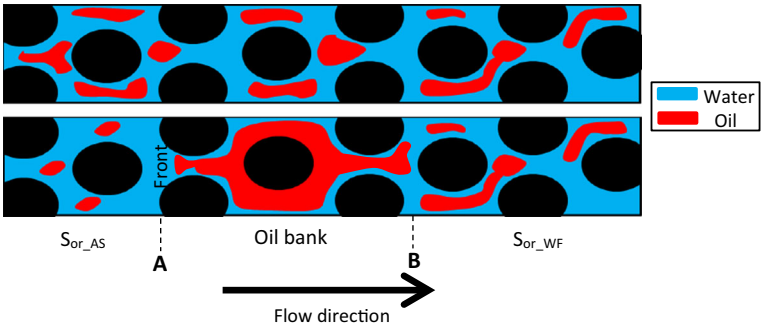

Fig. 14 Schematic overview of the proposed oil mobilisation mechanism by the injected AS slug. The top sketch presents the situation after water flooding (at S_{or_WF}) and the bottom one shows the situation during AS slug injection where the oil bank/AS slug front has reached approximately one-fourth of the core. **a** and **b** Refer to the trailing edge and leading edge, respectively

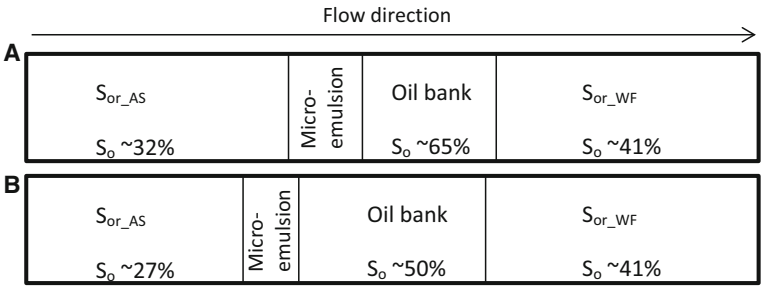

Fig. 15 Schematic representation of static oil saturation models related to the condition after AS slug injection for Exp. 4 (**a**) and Exp. 5 (**b**)

IFT larger quantities of mobilised oil were available for oil coalescence, and consequently, less oil was accessible for solubilisation.

4.5 Displacement of the Oil Bank: Foaming Mechanism

Our results proved that stable foam could be generated at higher S_o (oil bank) rather than at low S_o (upstream of oil bank). Considering this observation with caution since the experiments were done at specific conditions (model oil, clean sandstone, etc.), this surprising result strongly suggests that the existence of stable pseudo-emulsion films allowed foam lamellae transport in presence of oil droplets. For further discussion on foaming mechanisms, we consider the schematic representation of the averaged static saturation distributions at the end of AS slug injection for both ASF core-floods (Fig. 15). The physical mechanisms responsible for foam generation are snap-off, lamellae division and leave behind (Kovscek and Radke 1994). First let us consider the absence of stable foam generation upstream of the oil bank. The common consensus is that two conditions must be satisfied for foam generation in porous media: (1) sufficient amount of foaming agent present in the aqueous phase, and (2) the pressure gradient should exceed a critical value, ∇p_{min} (Rossen and Gauglitz 1990; Gauglitz et al. 2002). Most probably, the local pressure drop, in combination with the presence of S_{or_AS}, in the upstream section was too low for lamellae division to occur (Fig. 8), hence the

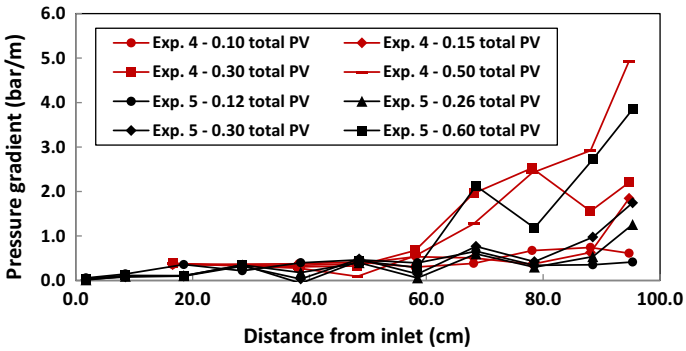

Fig. 16 Constructed pressure gradient profiles for Exp. 4 and 5. Profiles were constructed by pinpointing the pressure drop over a certain section to its centre. After approximately 0.12 ± 0.02 total PV (Exp. 4) and 0.26 ± 0.02 total PV (Exp. 5), pressure gradients started to increase downstream due to foam generation

presence of partly overriding gas bubbles (Fig. 10). A more uniform gas bubble distribution was generated at a distance of 50 ± 1 cm (Exp. 4) and 62 ± 1 cm (Exp. 5) from the inlet, corresponding to the increase in total pressure drop at, respectively, 0.12 ± 0.02 total PV (Exp. 4) and at 0.26 ± 0.02 total PV (Exp. 5) (Figs. 8 and 16). At those injection times, the trailing edge of the oil bank already passed the distances of 50 ± 1 cm and 62 ± 1 cm for Exp. 4 and 5, respectively (Fig. 9). We propose that the presence of a potential micro-emulsion phase upstream of the trailing edge, as found in the effluent, might contribute, together with oil bank remnants, to the foaming characteristics observed. Once the co-injected gas reached the potential micro-emulsion zone, effective porosity decreased, gas and liquid superficial velocities increased, and accordingly, the local pressure drop increased as well. This may be the trigger responsible for initiating lamellae division, leading to a more uniform gas bubble distribution as seen in Fig. 10.

The oil mobilisation and foaming mechanisms discussed above should be validated by performing experiments enabling the study of pore-scale processes such as dedicated microfluidic experiments. Such experiments may also reveal the cause of the varying distinct shapes of the oil bank between (near-)optimum and under-optimum salinity flooding.

5 Conclusions

Gas flooding and foam-assisted chemical flooding processes were investigated using a model oil and Bentheimer sandstone cores. Immiscible gas, water-alternating-gas (WAG) and alkaline–surfactant–foam (ASF) processes were studied by well-controlled CT-assisted core-flood experiments. ASF core-floods were conducted both at under-optimum and at (near-)optimum salinity conditions. Our findings have led to the following main conclusions:

- WAG injection increased oil recovery over continuous gas flooding by $8 \pm 2\%$ of the oil initially in place (OIIP), yielding an ultimate recovery factor of $59 \pm 4\%$ of the OIIP. The establishment of trapped gas, reducing gas mobility, is a key factor for the incremental oil recovered by WAG.
- The designed AS slug formulation lowered the oil–water interfacial tension by a factor of 130 and 540 for under-optimum and (near-)optimum salinity conditions, respectively. The AS drive formulation showed good foaming characteristics in bulk.

- Lowering oil–water interfacial tensions favours the mobilisation of residual oil to waterflood, promoting the formation of an oil bank. At (near-)optimum salinity, the oil bank formed was more uniform and elongated compared to the oil bank developed at under-optimum salinity conditions.
- Co-injection of AS drive solution and N_2 in presence of n-hexadecane generated weak foams. Foam strength surged upon hitting the oil bank, leading to highly effective displacement of the banked oil. The suggested mechanism implies that the presence of a potential micro-emulsion phase, in combination with oil bank remnants, controls foaming characteristics.
- Ultimate oil recovery at under-optimum ASF flooding was rather similar to that for WAG ($60 \pm 5\%$ of the OIIP). However, the ultimate recovery for ASF at (near-)optimum salinity was higher by $15 \pm 5\%$ of the OIIP, proving the higher effectiveness of oil mobilisation and displacement.
- Performing ASF flooding at (near-)optimum salinity increased the produced clean oil–emulsified oil ratio over under-optimum flooding with roughly a factor 10.

Acknowledgements This study is the result of collaboration between Delft University of Technology, Universiti Teknologi Petronas, Petronas and Shell. We are grateful to Petronas and Shell for funding the project. The authors thank Petronas for the supply of materials and data.

Appendix A: Pressure Drop Versus Oil Bank Shape During AS Slug Injection

In order to study the relationship between the observed pressure drops (Fig. 6) and corresponding shapes of the oil bank (Fig. 7) Darcy's law, in combination with Brooks and Corey model for relative permeabilities (Brooks and Corey 1966), was applied to simple test cases presented in Table 10 and Fig. 17. The formulas used are shown below. A simplified one dimensional Darcy's law was assumed:

$$\Delta P = u_{\text{tot}} \left(\frac{f_{\text{o}} \mu_{\text{o}}}{k_{\text{ro}} k} + \frac{f_{\text{w}} \mu_{\text{w}}}{k_{\text{rw}} k} \right) L \tag{A.1}$$

where ΔP, u_{tot}, μ_{a}, k_{ra}, k, f_{a} and L represent the pressure drop, total superficial velocity, viscosity of phase a, relative permeability of phase a, absolute permeability to brine, fractional flow of phase a and the core length, respectively. Subscripts o and w refer to the oil and water phases, respectively. The relative permeabilities are derived using Brooks and Corey model:

$$k_{\text{ro}} = k_{\text{ro}^*} \left(\frac{S_{\text{o}} - S_{\text{or}}}{1 - S_{\text{or}} - S_{\text{wc}}} \right)^{n_{\text{o}}} \tag{A.2}$$

$$k_{\text{rw}} = k_{\text{rw}^*} \left(\frac{S_{\text{w}} - S_{\text{wc}}}{1 - S_{\text{or}} - S_{\text{wc}}} \right)^{n_{\text{w}}} \tag{A.3}$$

where k_{ra^*} and n_{a} represent the end-point relative permeability and the Brooks–Corey exponent for phase a, respectively. Pressure drops are derived using a space interval of 1.0 cm

Table 10 Parameters used to derive the pressure drop analytically for the two model cases shown in Fig. 17

L (m)	U_{tot} (m/s)	μ_{o} (Pa s)	μ_{w} (Pa s)	k (m^2)	k^*_{ro}	k^*_{rw}	S_{or}	S_{wc}	n_{o}	n_{w}
0.01	2.09E−06	3.38E−3	1.07E−3	3.2E−12	0.51	0.13	0.09	0.22	1	2

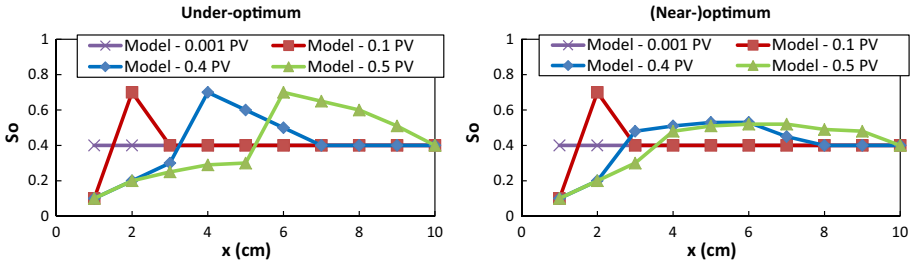

Fig. 17 Simplified test cases that represent the development of the oil bank during AS slug injection at, respectively, under-optimum (left) and (near-)optimum (right) salinity conditions. Note that the development of the oil bank in the model has similar characteristics as the observations made during the performed experiments (Fig. 7). Water saturations were calculated using $1 - S_o$. The total amount of oil present at each time was held constant; assuming no oil being produced

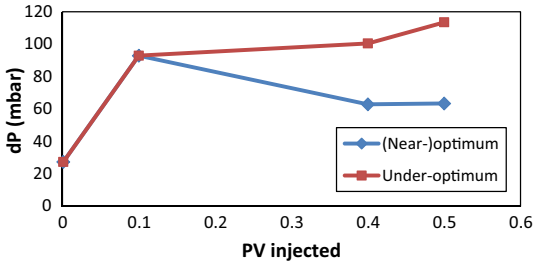

Fig. 18 Total pressure drop profiles constructed for the two simplified models shown in Fig. 17. Note that qualitatively it represents the observations made during AS slug injection in Exp. 4 and 5

(i.e. for every cm pressure drops are calculated using the saturation distributions presented in Fig. 17). Note that we only address the variations in phase saturations, i.e. relative permeabilities, and its impact on the total pressure drop.

The derived total pressure drop profiles, i.e. the sum of pressure drops calculated over 1.0 cm sections, are shown in Fig. 18. Qualitatively they are similar to the observed pressure drops during AS slug injection in the experiments conducted (Fig. 6): a sharp increase followed by a more gradual increase (under-optimum) and a sharp increase followed by a gradual decrease [(near-)optimum]. The higher pressure drops during under-optimum compared to (near-)optimum injection is due to the relatively high peak S_o (close to $1 - S_{wc}$) within the oil bank. The reduction in water mobility, $\frac{k_{rw}k}{\mu_w}$, has the greatest impact on the increase in pressure drop. Furthermore, as injection continued at under-optimum salinity conditions, the oil bank grew continuously while maintaining its peak S_o, thus enlarging the total pressure drop.

At (near-)optimum salinity injection first a sharp increase in pressure drop is seen due to the formation of the sharp oil bank at early injection times (similar to under-optimum salinity injection). Afterwards, peak S_o reduced and the oil bank became more uniform. The constant, relatively low, S_o of around 0.5 revealed a slight reduction in total pressure drop as the peak S_o within the oil bank was reduced significantly. This effect could not be compensated by the growth of the oil bank. Further development of the oil bank hardly effects the pressure drop as the expansion at the leading edge is neutralised by a slight reduction in peak S_o.

References

Aderangi, N., Wasam, D.T.: Coalescence of single drops at a liquid–liquid interface in the presence of surfactants/polymers. Chem. Eng. Commun. **132**(1), 207–222 (1995)

Andrianov, A.I., Liu, M.K., Rossen, W.R.: Sweep efficiency in CO_2 foams simulations with oil. In: IOR 2011-16th European Symposium on Improved Oil Recovery (2011)

Aronson, A.S., Bergeron, V., Fagan, M.E., Radke, C.J.: The influence of disjoining pressure on foam stability and flow in porous media. Colloids Surf. A Physicochem. Eng. Asp. **83**(2), 109–120 (1994)

Blunt, M., Zhou, D., Fenwick, D.: Three-phase flow and gravity drainage in porous media. Transp. Porous Media **20**(1–2), 77–103 (1995)

Brooks, R.H., Corey, A.T.: Properties of porous media affecting fluid flow. J. Irrig. Drain. Div. **92**, 61–88 (1966)

Buckley, S.E., Leverett, M.: Mechanism of fluid displacement in sands. Trans. AIME **146**(1), 107–116 (1942)

Castanier, L.M.: Introduction to computerized X-ray tomography for petroleum research. In: US Department of Energy Technical Report DOE/BC/14126-7. Stanford University, CA (USA). Petroleum Research Inst. (1988)

Chatterjee, J., Wasan, D.T.: A kinetic model for dynamic interfacial tension variation in an acidic oil/alkali/surfactant system. Chem. Eng. Sci. **53**(15), 2711–2725 (1998)

Darcy, H.: Les fontaines publiques de la ville de Dijon: exposition et application. Victor Dalmont (1856)

Dietz, D.N.: A theoretical approach to the problem of encroaching and by-passing edge water. In: Akad. Van Wetenschappen, Amsterdam. Proc. B vol. 56, pp. 83–92 (1953)

Dong, M., Foraie, J., Huang, S., Chatzis, I.: Analysis of immiscible water-alternating-gas (WAG) injection using micromodel tests. J. Can. Pet. Technol. **44**(2), 17–25 (2005)

Du, D., Zitha, P.L.J., Uijttenhout, M.G.: Carbon dioxide foam rheology in porous media: a CT scan study. SPE J. **12**(2), 245–252 (2007)

El Din Saad Ibrahim, A.S.: Investigation of the mobilization of residual oil using micromodels. Soc. Pet. Eng. (2009). https://doi.org/10.2118/129515-STU

Farajzadeh, R., Andrianov, A., Bruining, J., Zitha, P.L.J.: Comparative study of CO_2 and N_2 foams in porous media at low and high pressure-temperatures. Ind. Eng. Chem. Res. **48**(9), 4542–4552 (2009)

Farajzadeh, R., Andrianov, A., Zitha, P.L.J.: Investigation of immiscible and miscible foam for enhancing oil recovery. Ind. Eng. Chem. Res. **49**(4), 1910–1919 (2010)

Fatemi, M.S., Sohrabi, M.: Experimental investigation of near-miscible water-alternating-gas injection performance in water-wet and mixed-wet systems. Soc. Pet. Eng. (2013). https://doi.org/10.2118/145191-PA

Fayers, F.J.: Enhanced Oil Recovery: Proceedings of the Third European Symposium on Enhanced Oil Recovery. Elsevier Science Publishing Company, Bournemouth (1981)

Gauglitz, P.A., Friedmann, F., Kam, S.I., Rossen, W.R.: Foam generation in homogeneous porous media. Chem. Eng. Sci. **57**, 4037–4052 (2002)

Guo, H., Zitha, P.L.J., Faber, R., Buijse, M.: A novel alkaline/surfactant/foam enhanced oil recovery process. SPE J. **17**(4), 186–195 (2012)

Hagoort, J.: Oil recovery by gravity drainage. Soc. Pet. Eng. **2**, 139–150 (1980). https://doi.org/10.2118/7424-PA

Hecht, E.: Optics, 4th edn. Addison-Wesley, Boston (2001)

Hirasaki, G.J., Zhang, D.L.: Surface chemistry of oil recovery from fractured oil-wet carbonate formations. SPE J. **9**(2), 151–162 (2004)

Hirasaki, G.J., Miller, C.A., Puerto, M.: Recent advances in surfactant EOR. SPE J. **16**(4), 889–907 (2011)

Hosseini-Nasab, S.H., Zitha, P.L.J.: Systematic phase behaviour study and foam stability analysis for optimal alkaline/surfactant/foam enhanced oil recovery. In: IOR 2015-18th European Symposium on Improved Oil Recovery (2015)

Howe, A.M., Clarke, A., Mitchell, J., Staniland, J., Hawkes, L.A.: Visualising surfactant EOR in core plugs and micromodels. Soc. Pet. Eng. (2015). https://doi.org/10.2118/174643-MS

Huang, D.D., Honarpour, M.M.: Capillary end effects in coreflood calculations. J. Pet. Sci. Eng. **19**(1–2), 103–117 (1998)

Janssen, M.T.G., Zitha, P.L.J., Pilus, R.M.: Oil recovery by alkaline-surfactant-foam (ASF) flooding: effect of drive foam quality on oil bank propagation. Soc. Pet. Eng. (2018). https://doi.org/10.2118/190235-MS

Jong, S., Nguyen, N.M., Eberle, C.M., Nghiem, L.X., Nguyen, Q.P.: Low tension gas flooding as a novel EOR method: an experimental and theoretical investigation. Soc. Pet. Eng. (2016). https://doi.org/10.2118/179559-MS

Kang, W., Liu, S., Meng, L., Cao, D., Fan, H.: A novel ultra-low interfacial tension foam flooding agent to enhance heavy oil recovery. Soc. Pet. Eng. (2010). https://doi.org/10.2118/129175-MS

Khorshidan, H., James, L.A., Butt, D.S.: The role of film flow and wettability in immiscible assisted gravity drainage. In: International Symposium of the Society of Core Analysts, Colorado, USA (2016)
Klitzing, R.V., Espert, A., Asnacios, A., Hellweg, T., Colin, A., Langevin, D.: Forces in foam films containing polyelectrolyte and surfactant. Colloids Surf A Physicochem Eng Asp **149**(1), 131–140 (1999)
Kovscek, A.R., Radke, C.J.: Fundamentals of foam transport in porous media. In: Foams: Fundamentals and Applications in the Petroleum Industry, pp. 115–163 (1994)
Lake, L.W.: Enhanced Oil Recovery. Prentice-Hall, Englewood Cliffs (1989)
Laplace, P.: Mécanique celeste 10. Supplement to the tenth edition (1806)
Lide, D.R.: CRC Handbook of Chemistry and Physics. CRC Press, Boca Raton (2012)
Liu, S.H., Hirasaki, G.K., Miller, C.A.: Favorable attributes of alkaline-surfactant-polymer flooding. SPE J. **12**(1), 5–6 (2008)
Oren, P.E., Billiotte, J., Pinczewski, W.V.: Mobilization of waterflood residual oil by gas injection for water-wet conditions. Soc. Pet. Eng. (1992). https://doi.org/10.2118/20185-PA
Peksa, A.E., Wolf, K.H.A., Zitha, P.L.J.: Bentheimer sandstone revisited for experimental purposes. Mar. Pet. Geol. **67**, 701–719 (2015)
Rossen, W.R.: Foams in enhanced oil recovery. In: Prud'homme, R.K., Khan, S. (eds.) Foams: Theory Measurements and Applications. Marcel Dekker, New York (1996)
Rossen, W.R., Gauglitz, P.A.: Percolation theory of creation and mobilization of foams in porous media. AIChE **36**, 1176–1188 (1990)
Rossen, W.R., Van Duijn, C.J., Nguyen, Q.P., Vikingstad, A.K.: Injection strategies to overcome gravity segregation in simultaneous gas and liquid injection into homogeneous reservoirs. Soc. Pet. Eng. (2006). https://doi.org/10.2118/99794-PA
Sebastian, H.M., Lawrence, D.D.: Nitrogen minimum miscibility pressures. Soc. Pet. Eng. (1992). https://doi.org/10.2118/24134-MS
Shabib-Asl, A., Ayoub, M.A., Alta'ee, A.F., Saaid, I.B.M., Valentim, P.P.J.: Comprehensive review of foam application during foam assisted water alternating gas (FAWAG) method. Res. J. Appl. Sci. Eng. Technol. **8**(17), 1896–1904 (2014)
Shandrygin, A., Shelepov, V., Ramazanov, R., Andrianov, N., Klemin, D., Nadeev, A., Yakimchuk, I.: Mechanism of oil displacement during wag in porous media with micro-inhomogeneities. Soc. Pet. Eng. (2015). https://doi.org/10.2118/176629-MS
Sharma, B., Brigham, W.E., Castanier, L.M.: A Report on CT-Imaging Techniques for Two-Phase and Three-Phase In-Situ Saturation Measurements. Prepared for US Department of Energy, Stanford University (1997)
Shupe, R.D.: Chemical stability of polyacrylamide polymers. J. Pet. Technol. **33**(8), 1513–1529 (1981)
Simjoo, M., Dong, Y., Andrianov, A., Talanana, M., Zitha, P.L.J.: CT scan study of immiscible foam flow in porous media for enhancing oil recovery. Ind. Eng. Chem. Res. **52**(18), 6221–6233 (2013)
Srivastava, M., Zhang, J., Nguyen, Q.P., Pope, G.A.: A systematic study of alkali surfactant gas injection as an enhanced oil recovery technique. Soc. Pet. Eng. (2009). https://doi.org/10.2118/124752-MS
Szlendak, S.M., Nguyen, N.M., Nguyen, Q.P.: Laboratory investigation of low-tension-gas flooding for improved oil recovery in tight formations. SPE J. **18**(5), 851–866 (2013)
Talebian, S.H., Masoudi, R., Tan, I.M., Zitha, P.L.J.: Foam assisted CO_2-EOR: a review of concept, challenges, and future prospects. J. Pet. Sci. Eng. **120**, 202–215 (2014)
Tang, S., Tian, L., Lu, J., Wang, Z., Xie, Y., Yang, X., Lei, X.: A novel low tension foam flooding for improving post-chemical-flood in Shuanghe oilfield. Soc. Pet. Eng. (2014). https://doi.org/10.2118/169074-MS
Treiber, L.E., Archer, D.L., Owens, W.W.: A laboratory evaluation of the wettability of fifty oil producing reservoirs. SPE J. **12**(6), 531–540 (1972)
Vizika, O.: Effect of the spreading coefficient on the efficiency of oil recovery with gravity drainage. In: Enhanced Oil Recovery Symposium, 205th National Meeting. American Chemical Society, Denver, CO, March 28–April 2 (1993)
Wasan, D.T., Shah, S.M., Aderangi, N., Chan, M.S., McNamara, J.J.: Observations on the coalescence behaviour of oil droplets and emulsion stability in enhanced oil recovery. Soc. Pet. Eng. (1978). https://doi.org/10.2118/6846-PA
Winsor, P.A.: Solvent properties of amphiphilic compounds. Butterworths Scientific Publications. Ltd., London (1954)
Young III, T.: An essay on the cohesion of fluids. Philos. Trans. R. Soc. Lond. **95**, 65–87 (1805)
Zhang, Y.P., Sayegh, S.G., Luo, P., Huang, S.: Experimental investigation of immiscible gas process performance for medium oil. Soc. Pet. Eng. (2010). https://doi.org/10.2118/133203-PA
Zhu, T., Ogbe, D.O., Khataniar, S.: Improving the foam performance for mobility control and improved sweep efficiency in gas flooding. Ind. Eng. Chem. Res. **43**(15), 4413–4421 (2004)

Zitha, P.L.J., Du, D.X.: A new stochastic bubble population model for foam flow in porous media. Transp. Porous Media **83**(3), 603–621 (2010)
Zitha, P.L.J., Nguyen, Q.P., Currie, P.K., Buijse, M.A.: Coupling of foam drainage and viscous fingering in porous media revealed by X-ray computed tomography. Transp. Porous Media **64**(3), 301–313 (2006)

Publisher's Note Springer Nature remains neutral with regard to jurisdictional claims in published maps and institutional affiliations.